Stony Brook University

Variations of Thermally Sprayed Materials by Means of Coupled Property Response

A Thesis Presented

by

Christopher Jon Jensen

to

The Graduate School

in Partial Fulfillment of the

Requirements

for the Degree of

Master of Science

in

Materials Science and Engineering

Stony Brook University

December 2011

Stony Brook University

The Graduate School

Christopher Jon Jensen

We the thesis committee for the above candidate for the

Master of Science degree, hereby recommend

acceptance of this thesis

Professor Sanjay Sampath - Thesis Advisor

Professor, Department of Materials Science and Engineering

Professor Herbert Herman

Distinguished Professor Emeritus, Department of Materials Science and Engineering

Professor Christopher Weyant

Assistant Professor, Department of Materials Science and Engineering

This thesis is accepted by the Graduate School

Lawrence Martin

Dean of the Graduate School

Abstract of the Thesis

Variations of Thermally Sprayed Materials by Means of Coupled Property Response

by

Christopher Jon Jensen

Masters of Science

in

Materials Science and Engineering

Stony Brook University

2011

Emerging applications in electrical systems and components require the development of new and novel characterization methods for thermal spray coatings. Thermal spray is a complex process in which there are several multivariable dependencies. The relationship between processing and coating properties are often not fully understood.

Traditional mechanical properties are not sufficiently sensitive to characterize and classify the electrical response of a material and therefore new methods must be developed to fill the gaps in characterization methods related to electrical properties. It is necessary to develop new test methods which dynamically allow the determination of coating properties.

In the past, single property measurements have been achieved but it is the goal of this work to combine two properties in an attempt to gain insight into the microstructural changes of these complex coatings through coupled property response.

Particularly of interest is the variation in resistance as a function of mechanical strain via bending, as a function of thermal loading, and as a function of uniaxial mechanical tensile strain.

It has been demonstrated that monitoring the electrical resistance while imposing a mechanical strain through bending provides knowledge into the thermal spray coating, thus providing a useful qualitative characterization method. The splat to splat interfaces were determined to exhibit a similar affect to that of ceramics, namely slip and stick mechanisms. The slip and stick mechanism was apparent by the hysteresis displayed through cyclic loading of the sample.

To my beautiful wife

in appreciation of her loving support

and unfaltering patience

Table of Contents

List of Figures

List of Tables

Acknowledgment

I would like to take a moment to express my deepest gratitude to Professor Sanjay Sampath for his guidance and support. Thank you for sharing your vast thermal spray knowledge and for participating in countless discussions. Studying under Professor Sampath has truly been a privilege and an honor.

Thank you to my thesis committee members, Professor Herb Herman and Professor Chris Weyant for their thoughtful suggestions. Their comments and feedback have greatly improved the quality of this work.

It has been a pleasure working alongside the post doctoral research scientists and students of the Center for Thermal Spray Research. In particular, a special thanks to Dr. Brian Choi, Dr. Alfredo Valarezo, Gopal Dwivedi, Dr. Yang Tan, Lorena Bejarano, Dr. Kentaro Shinoda, and Travis Wentz for their openness to share past experiences, advice, and eagerness to lend a helping hand.

Chapter 1: Properties of Thermal Spray Coatings

1.1. Introduction

Thermal spray is a continuous process in which molten or semi-molten particles, on the order of 50 micrometers in diameter, are accelerated to high velocities. Gas streams direct the droplets causing impingement on a substrate where they experience a rapid spreading and solidification to form so-called "splats". The coating is built by the successive deposition of splats as shown in Figure 1-1 which provides a schematic overview of the thermal spray process. Due to the splat-by-splat build-up of the thermal spray process the deposit forms as a "brick-like" structure as illustrated in Figure 1-2. The thermal spray process allows for a vast range of materials to be deposited from low melting point polymers to high temperature ceramics as briefly outlined in Table 1-1.

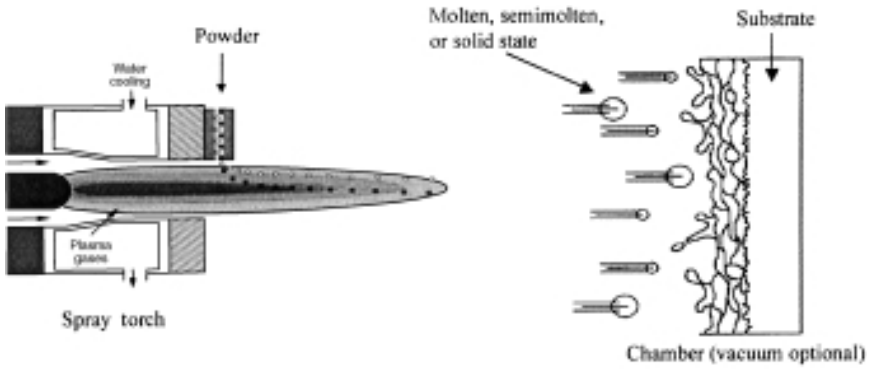

Figure 1-1: Schematic overview of the thermal spray process [2]

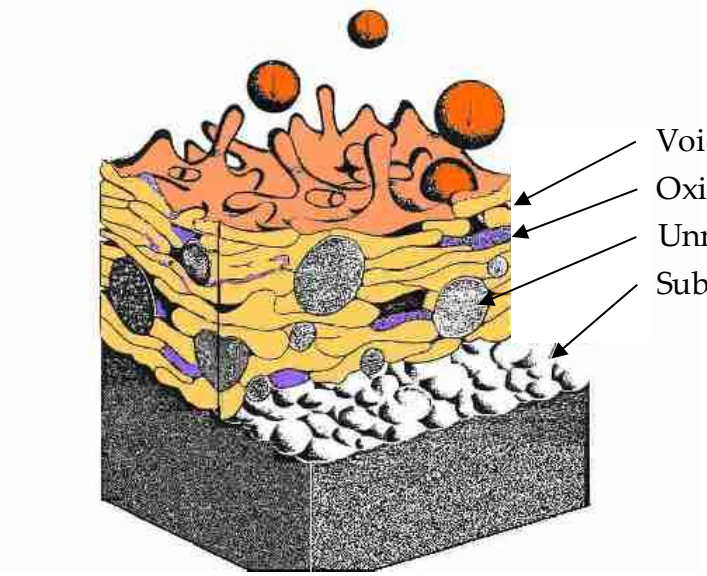

Figure 1-2: Illustration of the "brick-like" structure found in thermal spray coatings [1]

Table 1-1: Table of various materials and the complimentary thermal spray process employed

Wire Arc Spray	Flame Spray	High Velocity Oxy-Fuel	Atmospheric Plasma Spray
Zinc	Alumina	Tungsten Carbide	Molybdenum
Copper	Nickel Chrome	Tungsten Carbide Cobalt	Silicon
Aluminum	Molybdenum	Molybdenum Carbide	Yttria Stabilized Zirconia
Nickel	Polymers	Nickel Chrome	Alumina
Steel		Chromium Carbide	Chromium Oxide

While the deposit microstructure, and thus coating properties, are dependent on the spray material, they are also reliant on deposition parameters. The choice of deposition method, torch configuration, and process parameters allows the custom tailoring of coating properties where the connection between deposition process and coating properties are complex due to the numerous process parameters and their intricate relations.

1.2. Properties of Thermal Spray Coatings

Thermal spray coatings consist of cohesively bonded splats resulting from the impact, spreading, and rapid solidification of molten, or semi-molten, particles. The physical properties of the coatings rely on the cohesive strength between the splats, adhesion to the substrate, porosity, cracks and defects, as well as the grain structure within the splat. The high aspect ratio of the splats leads to an anisotropy of the coating properties in the direction parallel and perpendicular to the surface of the substrate.

The physical characteristics of the coating are primarily reliant on the impact conditions, predominantly the particle temperature and velocity. Factors such as substrate roughness, surface preparation, oxidation, and substrate temperature also affect the microstructure and properties of the coating [3-5].

Previous work completed at the Center for Thermal Spray Research has demonstrated that such coatings behave in complex ways. Specifically the coatings have demonstrated large anisotropy, inelasticity, and anelasticity [6-12].

1.3. Statement of the Problem and Thesis Objectives

The splat-based assemblage of thermal spray deposits results in a complex, defected structure consisting of pores, cracks and myriad array of separations. These lead to significant differences in properties from that of their bulk counterparts. A further challenge is the ability to measure properties of these complex systems due to limitations in size and form. Traditional methods of testing such as hardness, bond strength, and bending can be destructive and are not sensitive enough to characterize the subtle local and global variations within the thermal spray coating.

Recent research has shown that the spray layered structures also display unusual physical and mechanical properties such as large anisotropy, inelasticity and anelasticity. For example air plasma sprayed TiO2 displays novel anisotropic electrical responses in the as-sprayed state related to both the geometrical attributes of the microstructure as well as to the heterogeneous local oxidation states [13, 14]. Ceramic coatings display anelasticity in their thermo-mechanical and mechanical response while metallic coatings respond with inelastic deformation during loading [15-19]. Of further importance is the presence of residual stresses within the sprayed layers which can further alter the mechanical response of the system [20-24].

Many of the characterization techniques have examined singular properties of the coating and are somewhat limited in sensitivity to assess small changes occurring within these complex systems. One approach to overcome this issue is through coupled measurements; e.g., electrical and mechanical, electrical and thermal or even electrical-thermal and mechanical. It is envisioned that such a combined measurement strategy will allow for distilling small changes in global properties of these defected coatings and also enable a linkage to the state of the material and processing conditions. The goal of this thesis is to develop such a methodology for coupled property measurement of sprayed coatings. Notwithstanding the scientific interest, such an approach will allow enhanced characterization of functional coatings, for instance in thermal sprayed electrical conductors and thick film sensors.

The specific objectives of this thesis research were:

- Develop techniques for simultaneous measurement of electrical-thermal, electrical-mechanical properties of thermal sprayed materials including design of test specimens, test apparatus, and test protocols
- Identify critical issues in such a characterization approach including sensitivity, selectivity and repeatability.
- Explore materials and parametric effects for standard thermal spray systems.

Chapter 2: Thermal Spray Processes

2.1. Atmospheric Plasma Spray

Atmospheric Plasma Spray (APS) is a process in which a DC current generates an electric arc between a water cooled tungsten cathode and an annular water cooled copper anode. An arc gas usually consisting of an inert gas, such as nitrogen or argon, is mixed with an enthalpy-enhancing gas, such as hydrogen, and introduced from the rear of the torch where it swirls, forming a vortex [25].

Due to the electric arc between the anode and cathode a plasma flame is formed which axially rotates due to the momentum of the plasma gas. The temperature of the plasma just outside the torch can be in excess of 15,000 K for a typical DC torch operating at 40 kW [2]. The temperature of the plasma jet decreases rapidly as the distance from the nozzle increases. The powder feedstock to be deposited is introduced into the hottest part of the plasma flame either internally through the anode body or externally from the torch as shown in Figure 2-1.

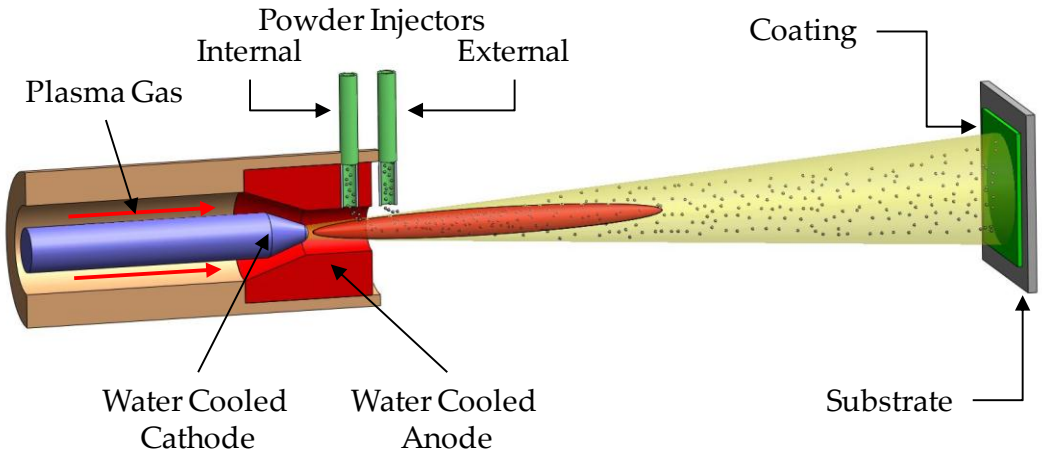

Figure 2-1: Schematic illustration of an Atmospheric Plasma Spray (APS) torch showing internal and external powder injection

The particles, roughly 50 micrometers in diameter, are melted in the flame and accelerated to speeds ranging from 100 m/s to 300 m/s towards the substrate. Once impacting on the substrate they undergo rapid spreading and solidification at cooling rates of one million °C/s.

The APS process has found wide spread use in the deposition of high temperature metals such as nickel and molybdenum as well as refractory ceramics such as aluminum oxide and zirconia-based ceramics. While plasma spray is capable of producing uniform coatings as thin as 2 micrometers, deposits of 50 micrometers or greater are more common.

2.2. High Velocity Oxy-Fuel Spray

High Velocity Oxy Fuel (HVOF) Spray is a variant of combustion spray in which the combustion flame is under compression and experiences free expansion upon exiting the torch. Utilizing an HVOF torch, process gases are able to reach velocities of Mach 4. The feedstock powder is introduced axially from the rear of the torch as shown in Figure 2-2. The particles are thus subjected to the high velocity gases which accelerate the particles to supersonic speeds.

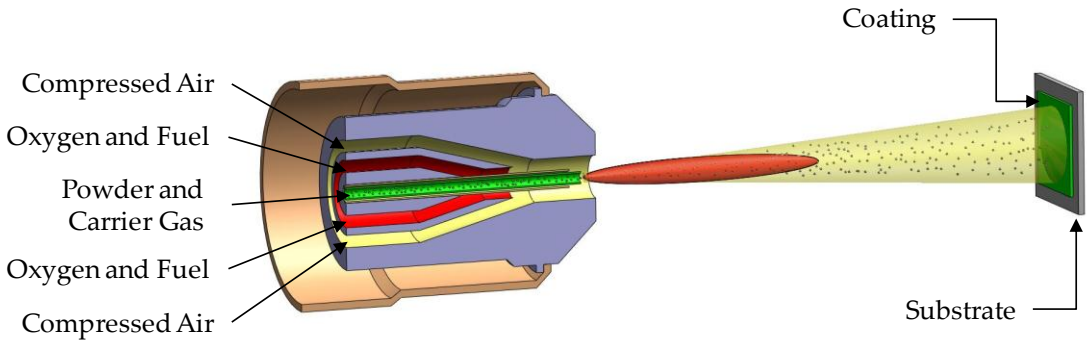

Figure 2-2: Schematic illustration of a High Velocity Oxy Fuel (HVOF) torch

Upon impact the particles spread forming extremely thin splats which bond very well to the substrate as well as to other splats in the vicinity. The HVOF process is able to produce coatings which are well bonded with deposit densities close to that of bulk materials.

While the process is capable of producing dense, well bonded coatings it is rather limited due to the relatively low temperatures attained by the combustion flame. Although the temperatures are relatively low it is possible to deposit some refractory ceramics such as alumina and spinel.

The HVOF process is used extensively in hardface coatings such as tungsten carbide cobalt which have hardness and wear resistances comparable to those of conventional bulk materials.

2.3. Cold Spray Deposition

In the Cold Spray deposition process, a high pressure inert gas, typically helium is pre-heated and passed through a converging/diverging nozzle (de Laval) where the gas reaches supersonic speeds. With the assistance of a high pressure powder feeder solid particles are entrained in the gas flow where they experience acceleration and impingement on the substrate. An overview of the cold spray process is shown in Figure 2-3.

While the cold spray process does not require thermal energy, the solid particles bond to the substrate through ballistic collisions which cause spreading and subsequent deposit buildup [26, 27]. Deposits formed through cold spray processes are generally of higher purity due to minimal oxidation and feedstock degradations often associated with high temperatures.

Resulting from the high velocity impacts, cold spray coatings generally show compressive residual stresses compared to the tensile stresses observed for traditional lower velocity thermal spray processes in which a portion of the residual stress is caused by the rapid solidification of splats. [21, 28]

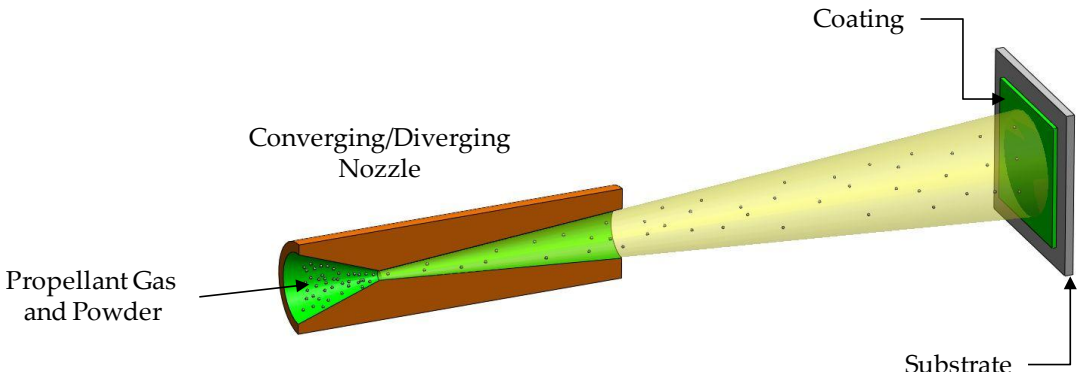

Figure 2-3: Schematic of a Cold Spray Deposition (CS) process

2.3.1. Sub-Sonic Solid State Deposition

Sub-Sonic Solid State Deposition, forwardly referred to as S4D, is a variant of cold spray technology. Similar to cold spray a high pressure inert gas, typically helium, travels through a powder feeder where a malleable metal powder becomes entrained in the gas flow. The gas then passes through a small straight bore nozzle where the particles reach speeds of approximately 160m/s on their path to the substrate.

A significant advantage of the S4D process is that it is able to deposit onto low melting point materials such as polymers. Additionally, through careful control of the process, it is possible to deposit via a direct write method in which fine features and geometries can be obtained [29-32].

2.4. Combustion Flame Spray

Combustion flame spray uses a fuel, such as acetylene, propylene, propane, natural gas, or hydrogen, to create a flame to which powder or wire feedstock is introduced. Either compressed air or oxygen can be used to increase

the flame temperature which is largely determined by the source materials melting temperature. Figure 2-4 shows a schematic of a typical combustion flame spray torch.

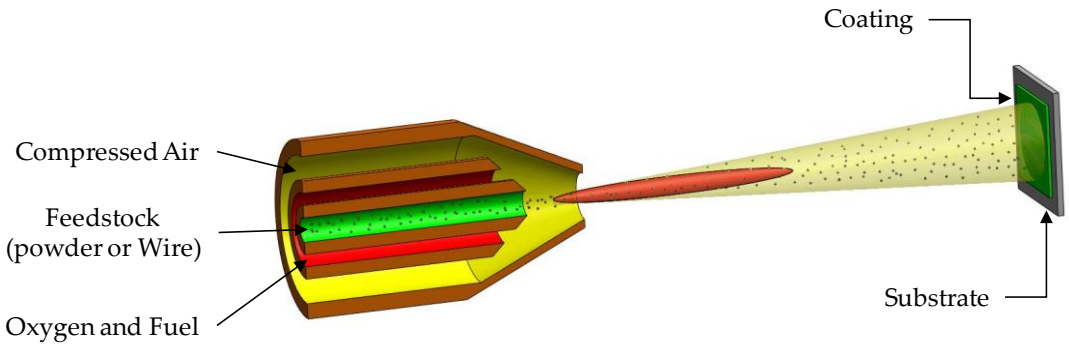

Figure 2-4: Schematic of Combustion Flame Spray torch

It has been found that coatings deposited via flame spray typically have lower density and weaker bond strength as compared to that of the APS or HVOF processes. Combustion flame spray operates at particle velocities of roughly 50 m/s and at relatively low temperatures due to the limitations of the combustion flame which results in higher oxide content, increased porosity, and inclusions in the coating and as a result flame spray coatings are often called low performance.

One advantage of using a low temperature flame spray process is in the ability to deposit polymer compounds. Generally used as a powder feedstock the deposition of polymers can be used in several fields from electrical insulation to nonskid coatings with low porosity.

A noteworthy application of the flame spray process is in spray and fuse coatings. The spray and fuse coatings are used where a hard, wear resistant, and impact resistant surface is desired, as in industrial machinery. First a wear resistant metallic coating is deposited onto the part via flame spray. Afterwards the part is placed in a furnace where the coating fuses to the substrate thus creating a dense metallurgical bond.

2.5. Wire Arc Spray

Wire arc spray is a process in which a pair of electrically conductive wires are melted by a high temperature, high current electric arc. Compressed air is used to atomize the molten material and propel the particles towards the substrate. Wire arc spray has an advantage in that two wires of different compositions can be co-deposited to form unique coatings. A typical illustration of a wire arc spray torch can be found in Figure 2-5.

Wire arc spraying is capable of depositing coatings at high rates which allows highly cost effective processing of large surface areas. For this reason a main application of wire arc spraying is in the deposition of corrosion protective materials such as aluminum and zinc for marine applications and infrastructure.

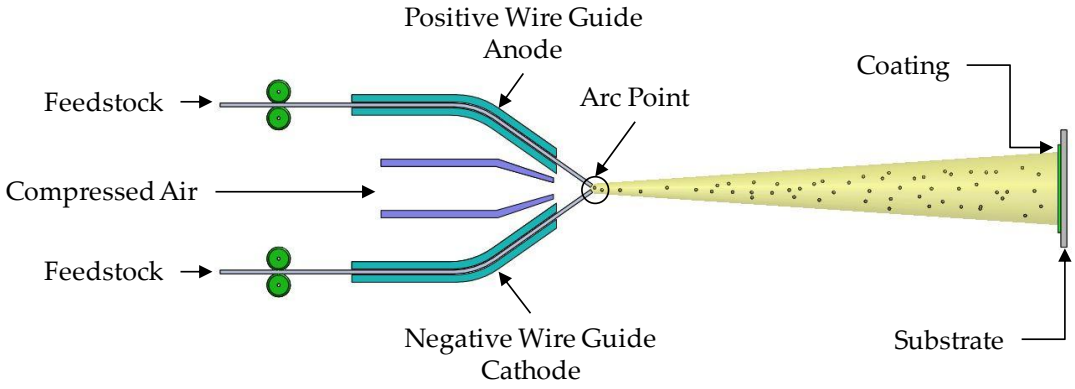

Figure 2-5: Schematic of Wire Arc Spray torch

2.6. Thermal Spray Processing Overview

A brief summary of thermal spray processes can be found in Table 2-1.

Table 2-1: Summary of thermal spray processes and key features [2]

Spray Type	Feed Type	Flame Temperature °C	Particle Velocity m/s	Materials	Microstructure	Applications
APS	Wire Powder	~5,000-25,000	80-300	Ceramics Metals	Porosity in ceramic deposits	Thermal barriers Insulators
HVOF	Powder	~3,000	~400-800	Metals Cermets Low-Melt Ceramics	High density High adhesion Compressive stresses	Wear protection
S4D	Powder	Room Temperature	~150	Ductile Metals	High density Compressive stresses	Conductors Reclamation Cladding
Flame Spray	Wire Powder	~3,000	~40-100	Metals Polymers Ceramics	High porosity Significant oxidation	Reclamation Corrosion protection
Wire Arc Spray	Wire	~3,000-6,000	50-150	Metals Cermets (cored wires)	Relatively dense Thick	Reclamation Wear coatings Corrosion protection

Chapter 3: Electrical Response as a Function of Strain via Bending

3.1. Introduction

A cantilever beam exposed to a force on the free end experiences a bending moment. This bending moment creates compressive and tensile stresses on either face of the beam perpendicular to the applied load as illustrated in Figure 3-1. From the illustration it is clear to see that the face on which the applied load is directly acting is in tension while the opposing face is in compression. Figure 3-1 also illustrates the neutral axis of the beam, the plane in which the tensile and compressive stresses cancel resulting in a stress free state.

The resulting strain has the potential to affect the resistance through the "brick-like" structure of the thermal spray coating in unique ways. In order to determine the effect and develop new test methods a series of thermally sprayed lines were deposited onto cantilever beams and subjected to an applied load. This experiment serves to exaggerate the interactions and help shed light on the microstructural changes in a new and unique way by monitoring the resistance of the thermal spray coating as a function of strain induced via bending.

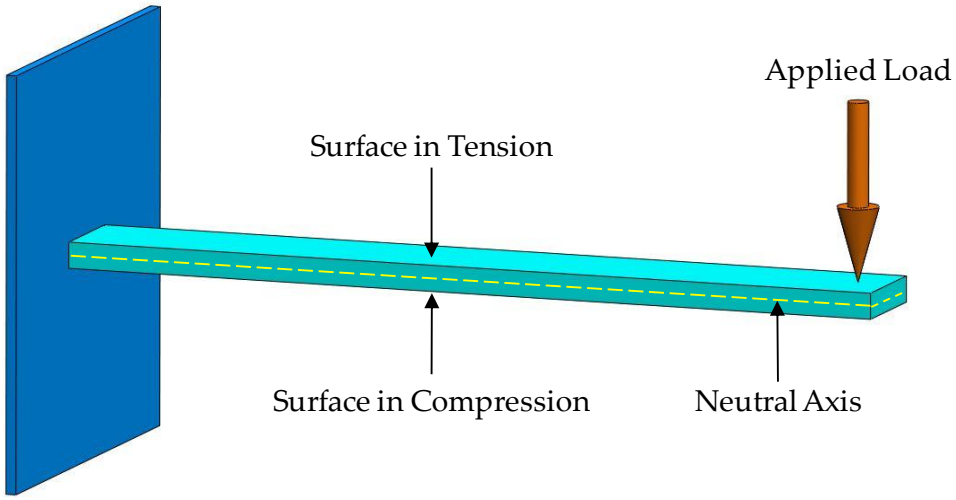

Figure 3-1: Illustration of a cantilever beam exposed to an applied load on the free end. Note the surface in which the applied load is directly acting on is in tension while the opposite side is in compression.

3.1.1. Cantilever Beam Geometry

In a cantilever beam with an applied load at the free end the bending moment varies linearly from zero at the point of load to a maximum at the fixed end. For a parallel sided beam, as shown in Figure 3-1, the axial stress on the beam surface is proportional to the bending moment which is expressed by

$$\sigma(x) = \frac{M(x)\, y}{I} = \frac{6\, P\, X}{b\, t^2} = \frac{P\, X}{Z}$$

Equation 3-1

where: M(x) = bending moment at point x

y = distance from the neutral axis to the point under consideration

I = moment of inertia for the beam

P = applied load

b = width of the beam

t = thickness of the beam

Z = section modulus of the beam

If the beam is parallel sided the cross-sectional area remains constant and as such the section modulus remains constant. From Equation 3-1 it is clear that the stress varies linearly from zero at the applied load to a maximum at the built in end. The surface of the cantilever beam is in a uniaxial stress state and therefore follows Hooke's Law such that strain is given by

$$\epsilon(x) = \frac{\sigma(x)}{E} = \frac{P\,X}{E\,Z}$$

Equation 3-2

where: E = elastic modulus

For the present experiment it is desirable to deposit and test the thermal spray coating where strain remains constant. From Equation 3-2 it can be seen that to create a beam in which there is a region of constant strain the section modulus must vary as a function of position as shown in Equation 3-3.

$$\frac{X}{Z(X)} = \frac{6\,X}{b(X)\,[t(X)]^2} = constant$$

Equation 3-3

To create a beam in which there is a section of constant strain it is necessary to vary the beam width as a function of X. A schematic of the constant strain cantilever with deposited thermal spray lines is shown in Figure 3-2.

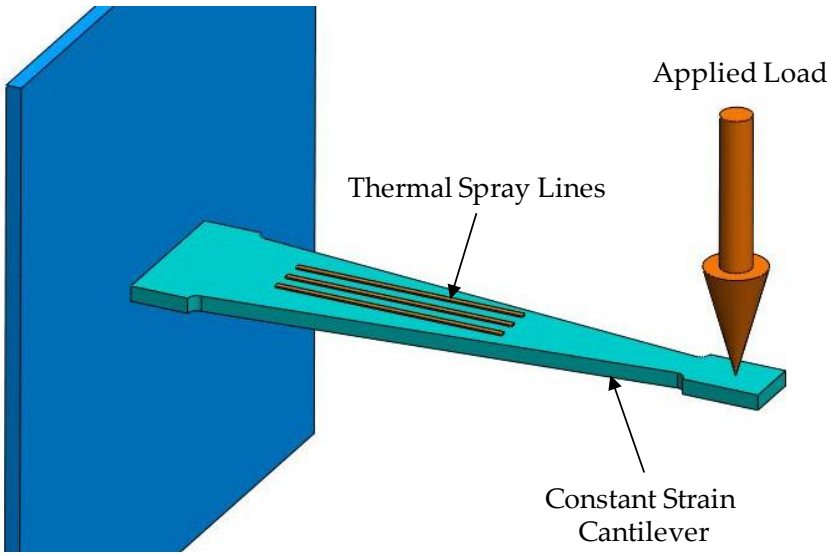

Figure 3-2: Illustration of constant strain cantilever with thermal spray lines subjected to a tensile strain resulting from the applied load

3.1.2. Measurement of Strain

The beams used for experimentation are that of a constant strain cantilever as described earlier. Taking advantage of the geometry it is appropriate to measure the strain on the surface of the beam using a traditional strain gauge. Figure 3-3 shows the constant strain cantilever with a strain gauge mounted in the center of the constant strain portion of the beam. Monitoring the resistance of the strain gauge allows for the direct measurement of the strain applied to the face of the beam in which the gauge is mounted on according to Equation 3-4.

$$\epsilon = \frac{\Delta R}{R_g \, GF}$$

Equation 3-4

where: ΔR = change in resistance of strain gauge

R_g = resistance of the undeformed strain gauge

GF = gauge factor of the strain gauge

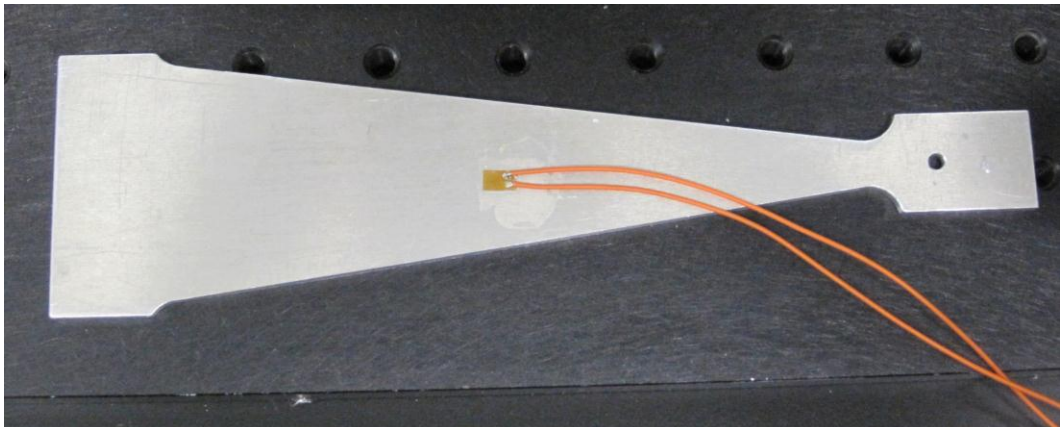

Figure 3-3: Illustration of constant strain cantilever with foil strain gauge mounted using cyanoacrylate glue

3.1.3. Calculation of Strain

The stress in a cantilever beam, where one end is rigidly fixed and the other subjected to an applied load, can be described using the elastic flexure formula which is given by

$$\sigma = -\frac{M\,y}{I}$$

Equation 3-5

where: M = moment at the point of loading

The moment for a cantilever beam is given by

$$M = -P\,(L - x)$$

Equation 3-6

where: P = the applied load at the free end

L = the length between the rigid support and free end

x = distance from the rigid support to the point under consideration

For a simple cantilever beam the distance between the neutral axis and point under consideration is given by

$$y = \frac{t}{2}$$

Equation 3-7

The moment of inertia for the beam is given by

$$I = \frac{1}{12}\, b\, (t^3)$$

Equation 3-8

Combining Equations 3-5 through 3-8 yields

$$\sigma_x = \frac{[-P(L-x)]\ \frac{t}{2}}{\frac{1}{12}\, b\, (t^3)} = \frac{6\, P\, (L-x)}{b\, t^3}$$

Equation 3-9

From Hooke's Law the stress in the beam is directly proportional to strain by the elastic modulus as shown by Equation 3-10.

$$\sigma_x = E\, \epsilon_x$$

Equation 3-10

Combining Equation 3-9 with Equation 3-10 the strain is given by

$$\epsilon = \frac{6\, P\, (L-x)}{E\, b\, t^2}$$

Equation 3-11

The applied load can be calculated in terms of deflection through the expression

$$\frac{d^2x}{dy^2} = \frac{M(x)}{E\,I}$$

Equation 3-12

Integration Equation 3-11 twice with the following boundary conditions

$$\frac{dy}{dx} = 0\ at\ x = 0$$

and

$$y = 0\ at\ x = 0$$

yields

$$y = \frac{P}{6\,E\,L}(x^3 - 3\,L\,x^2)$$

Equation 3-13

Substituting the deflection of the free end, δ_{end}, allows the calculation of the applied load given by

$$P = \frac{3\,\delta_{end}\,L\,I}{L^3}$$

Equation 3-14

Combining Equation 3-11 and 3-14 yields the strain as a function of beam end deflection.

3.2. Sample Preparation

In order to measure the electrical response of the thermal spray line it was necessary to insulate the electrically conductive aluminum beam from the line under test. This was accomplished by depositing a 100 μm spinel ($MgAl_2O_4$) layer onto the cantilever beam via APS using the Sulzer Metco F4 torch and Saint Gobain #171 powder. Immediately prior to deposition the sample was grit blasted using 40 μm diameter grit at 40 psi to provide a roughened, chemically active surface for the coating to adhere.

The sample was then mounted for deposition of the conductive layer. A shadow mask was used to facilitate the deposition of three discrete conductive lines of roughly 60mm length and 1mm width. Molybdenum-molybdenum carbide (Mo-Mo_2C) was then deposited by spraying Osram Sylvania SX274 powder through the shadow mask by means of APS. Table 3-1 shows the process parameters for the APS deposition of the spinel and moly-moly carbide.

Table 3-1: Deposition parameters for spinel insulator and Mo-Mo_2C conductive lines on constant strain cantilever beam

Material	Ar slpm	H2 slpm	Gun I Amp	Gun V Volt	Carrier/ Flow slpm	Feedrate g/min	Spray Dist mm	Raster Speed mm/s
MgAl2O4	47.5	6.0	550	61	Ar/3.0	30	100	500
Mo-Mo_2C	47.5	6.0	550	61	Ar/2.9	29	100	500

Lead wires were then attached to the conductive lines by several methods to determine the most suitable. Figure 3-4 illustrates lead wires connected by welding, wires cast in electrically conductive epoxy, and wire arc sprayed copper pads to allow soldering of lead wires to the thermal spray lines.

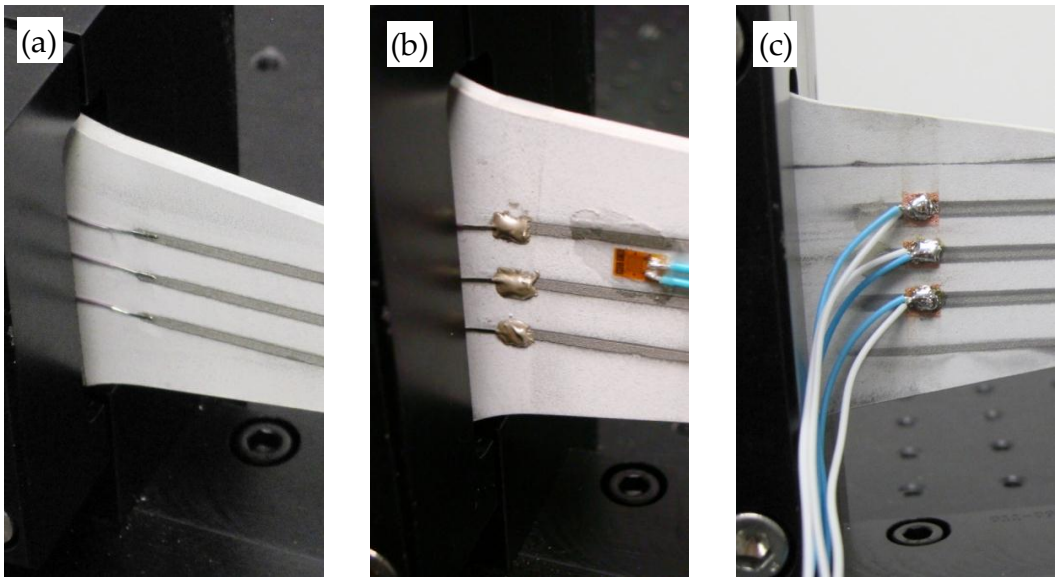

Figure 3-4: Illustration showing various lead wire bonding methods (a) welded leads, (b) leads cast in conductive epoxy, (c) leads soldered to wire arc sprayed copper pads

3.3. Experiment

3.3.1. Laser Displacement Sensor Calibration

In order to accurately measure the deflection of the cantilever's free end a Sunx ANR-12151 laser displacement sensor was employed. The particular sensor being used had a 100 mm operating range (i.e., +/- 50 mm). The setup was established in such a way that the cantilever beam was located at the center of the lasers operating range while in the unstrained state as shown in Figure 3-5. Note that the deflection causing the thermal spray line to experience a tensile strain is positive.

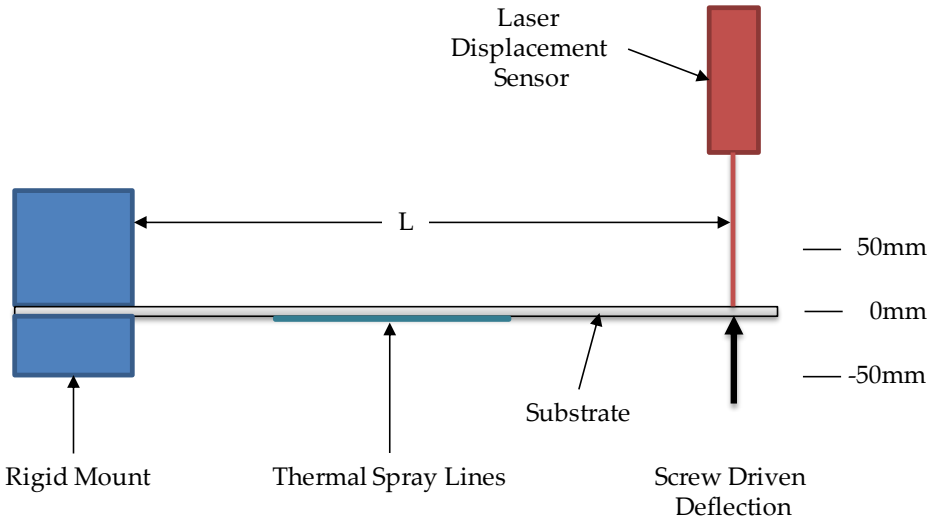

Figure 3-5: Schematic of cantilever beam location and laser displacement sensor operating range

A micrometer stage was positioned in front of the laser as shown in Figure 3-6 to allow precise incremental changes in displacement. The output voltage from the laser controller, Sunx ANR-5241, was recorded along with the resistance of the strain gauge using a Keithley 2700 series digital multimeter at five displacement positions to allow the calibration of the laser.

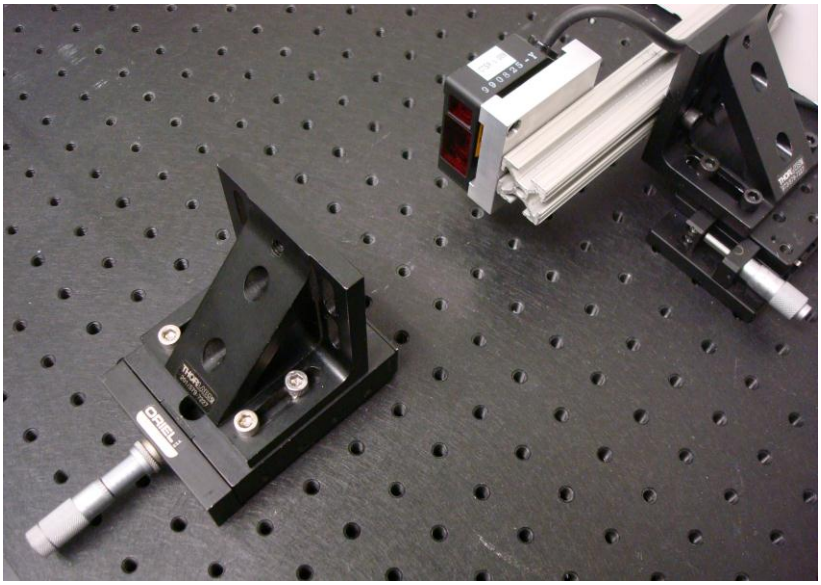

Figure 3-6: Illustration of laser displacement sensor calibration setup

3.3.2. Relation between Strain and Deflection

To accomplish the task of relating beam deflection to strain a foil strain gauge, Measurements Group Inc. EA-06-060-LZ-120, was mounted to an uncoated cantilever beam using cyanoacrylate glue. The resistance of the strain gauge was monitored as well as the output voltage from the laser controller while the deflection lead screw was slowly driven causing the beam to undergo bending. Figure 3-7 shows the experimental setup.

The strain gauge allowed the direct measurement of the strain in the beam (Equation 3-4) while the laser displacement sensor was used to calculate the strain based on the end deflection method (Equation 3-11). The two strains were compared to determine agreement.

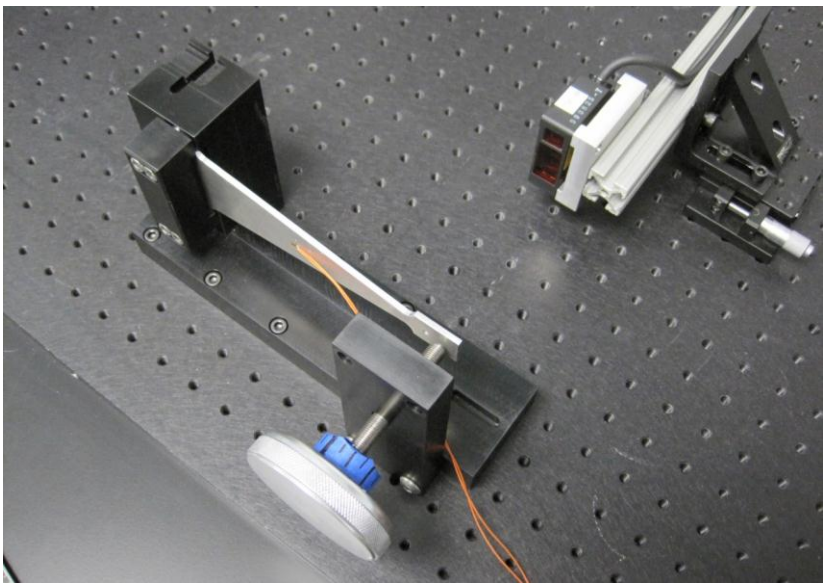

Figure 3-7: Illustration showing setup to determine the relationship between strain and displacement and thus measured versus calculated strain

3.3.3. Resistance as a Function of Strain

Once the system was calibrated and the relation between deflection and strain determined, the thermal spray sample was ready to be tested. The three independent lines were connected to a Keithley 2700 digital multimeter using a four wire test configuration for each line as illustrated in Figure 3-8. In this arrangement, two wires provide a 1 mA DC current which travels through the thermal spray line. The remaining two leads measure the voltage drop across the sample. Through Ohm's law the resistance of the line is calculated in the digital multimeter and automatically displayed. The four wire setup provides an advantage in that the resistance of the connections and lead wire is eliminated from the circuit. This is not the case when using a two wire test method where often the resistance of the lead wires and connections is significant compared to the resistance of the sample making it difficult to draw conclusions.

The sample was loaded to a 10 mm end deflection, corresponding to roughly 0.17% strain, by slowly turning the displacement lead screw. The strain was then slowly removed such that the beam could return to the unloaded state.

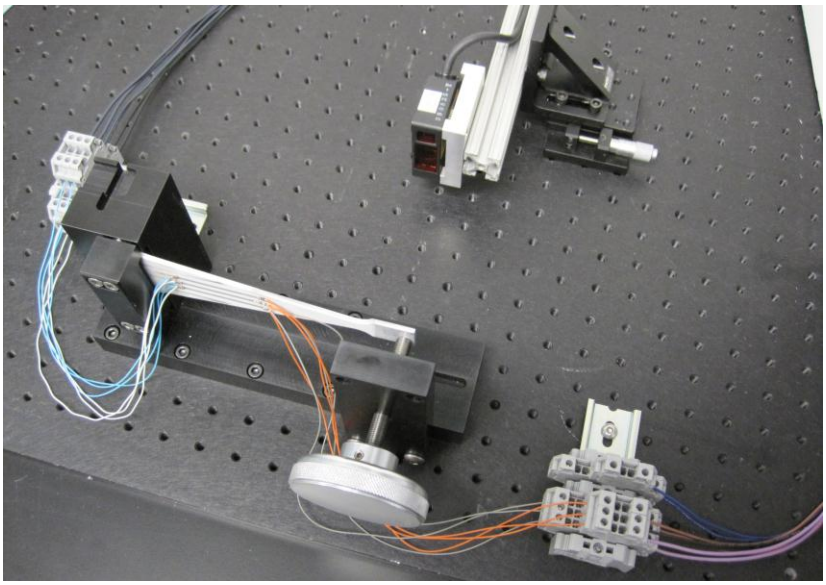

Figure 3-8: Illustration showing the test setup to measure resistance as a function of strain

3.3.4. Resistance Variations as a Function of Cyclic Strain

Monitoring the resistance of the thermal spray line over multiple strain cycles can provide insight into the microstructural changes as well as to the amount of damage induced in each cycle. The sample was loaded to a 10 mm deflection, corresponding to roughly 0.17% strain, by slowly turning the displacement lead screw. Once the desired strain was reached the sample was unloaded and brought back to the initial condition. This cycle was repeated such that the sample completed four full strain cycles.

3.3.5. Time Dependant Resistance

To determine if the thermal spray coating shows signs of low temperature time dependant creep the constant strain cantilever was used once again. In this experiment, the sample was loaded to 10 mm deflection where it was left untouched for nearly six hours at room temperature.

3.4. Results and Discussion

3.4.1. Laser Displacement Calibration

Figure 3-9 shows the plot of displacement versus laser controller output voltage. It is clear to see that the relationship is linear where the goodness of fit parameter, R squared, is 0.999993 showing an excellent linear correlation. The

equation of the line shown in Figure 3-9 is given by Equation 3-15 allowing displacement to be calculated from laser controller output voltage.

$$\delta = 31.52 * V + 60.72$$

Equation 3-15

where: δ = beam free end displacement

V = laser controller output voltage

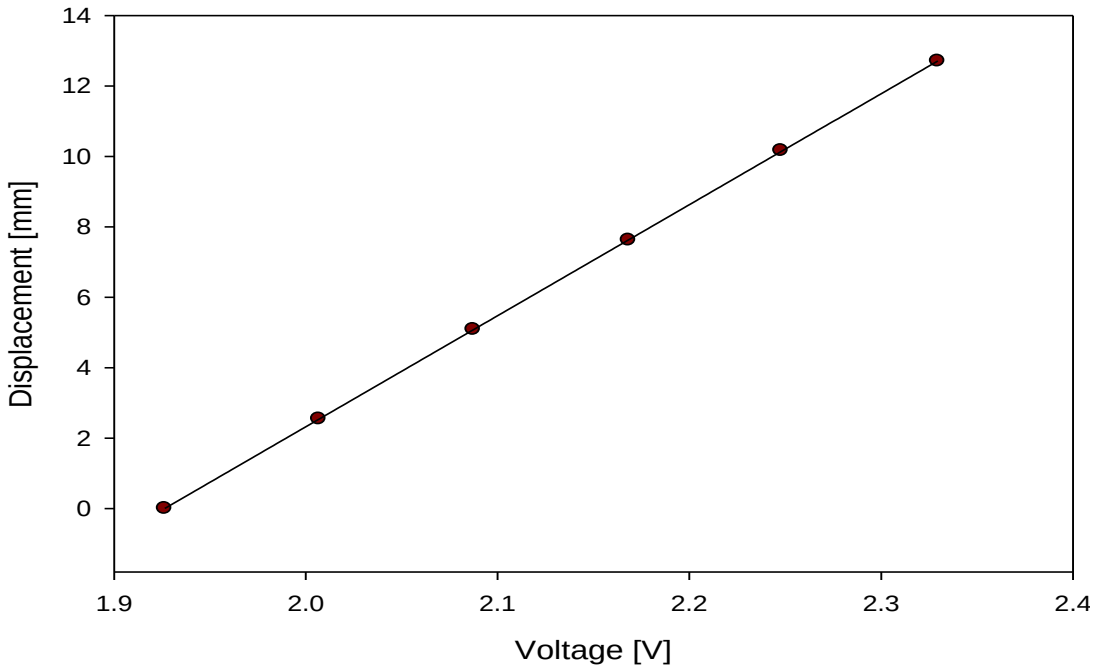

Figure 3-9: Plot of displacement versus laser controller output voltage

3.4.2. Strain-Displacement Relationship

Figure 3-10 shows the relationship between strain and displacement as well as the agreement between calculated and measured strain. As expected the measured strain in the increasing direction matches closely to that of the decreasing direction confirming that the experiment was within the elastic region of the beam. The difference between the measured and calculated strain is roughly 0.002328% strain at the maximum deflection which corresponds to a 3% absolute difference. Given the sources of error, such as the strain gauge, laser displacement sensor, controller output voltage, and Keithley meter, the data is in fair agreement confirming that strain calculated via the end deflection method is acceptable.

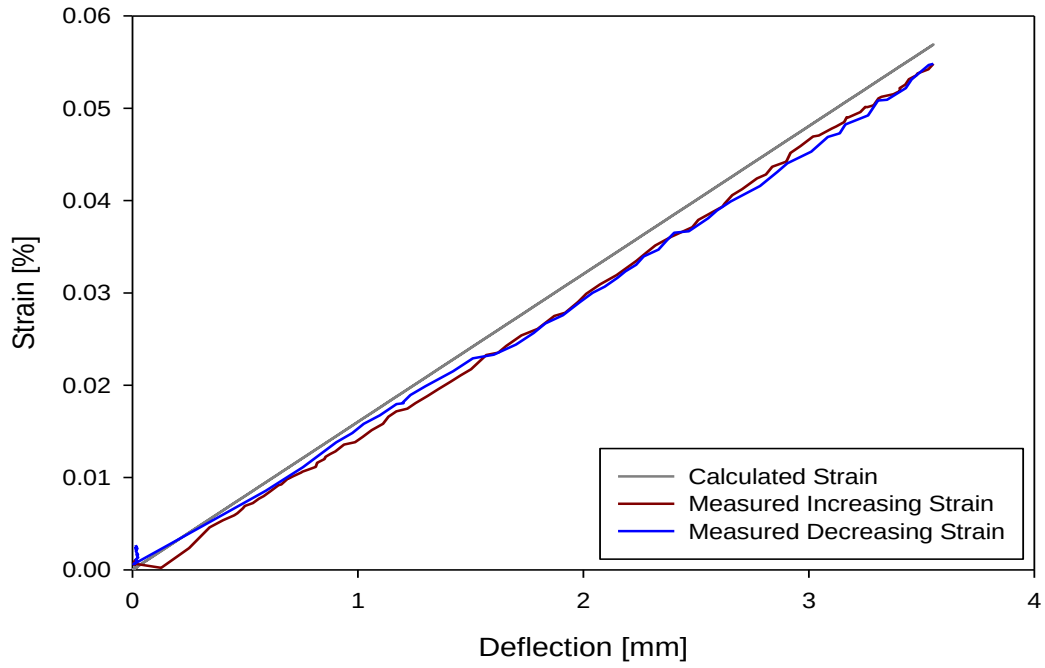

Figure 3-10: Plot showing relationship between strain and deflection in both the increasing and decreasing strains as well as the agreement between measured and calculated strain

3.4.3. Discussion of Resistance and Resistivity

Previous work has shown that large uncertainties arise from the geometrical variations in coating thickness and width when attempting to calculate electrical resistivity [33]. As a consequence the resistivity calculations can easily fluctuate by a factor of two or even an order of magnitude in some cases. The present work seeks to find relative changes rather than absolute numbers so electrical response will be discussed in terms of normalized resistance rather than resistivity.

It can be seen from Equation 3-16 that the resistivity is linearly dependant on cross-sectional area of the thermal spray line.

$$\rho = R\,\frac{A}{l}$$

Equation 3-16

where: ρ = electrical resistivity

R = resistance

A = cross-sectional area

l = line length

Figure 3-16 shows a 3D representation of the Mo-Mo_2C line deposited on the spinel coating using a Keyence VHX-500 Digital Microscope. The Keyence digital microscope takes a series of photographs of the sample with a slight shift in focal plane between images. The software then compiles the images to provide the digital 3D representation. The system is also capable of generating profile curves as found in Figure 3-17.

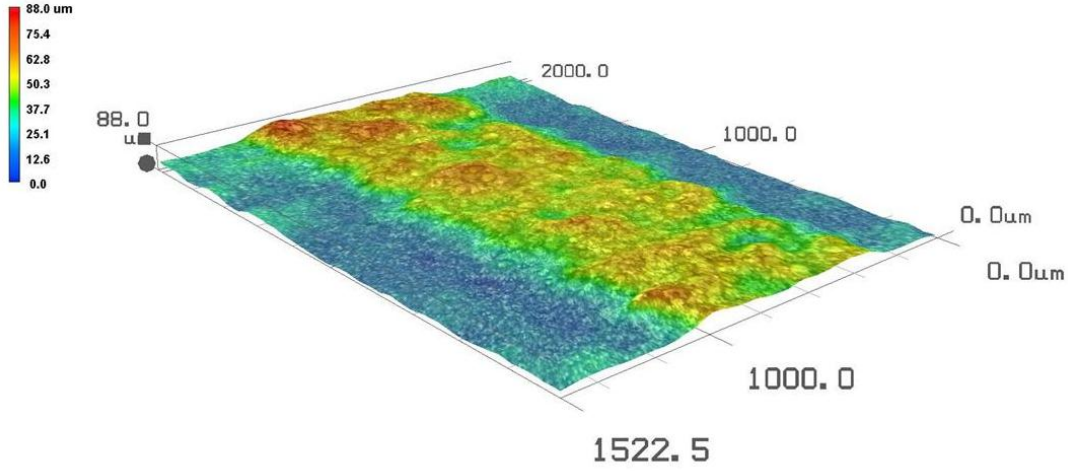

Figure 3-11: 3D compiled image of the Mo-Mo_2C deposited line on spinel coated constant strain cantilever showing line width of 0.9 mm and height of 50 µm

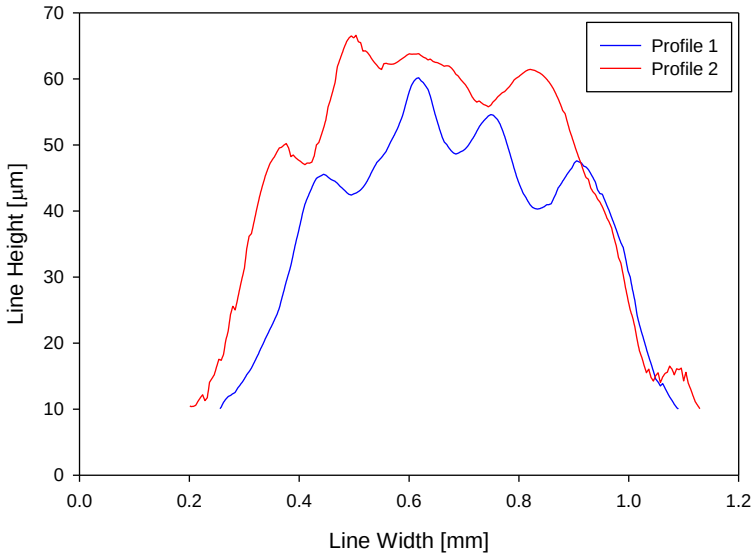

Figure 3-12: Cross-sectional profile of Mo-Mo_2C thermal spray line

Table 3-2 briefly demonstrates how the variance of the thermal spray coating can cause a wide range in resistivity values. Data shown is for line 2 of the Mo-Mo_2C sample taken over a 2 mm range. Also illustrated is that the cross-sectional area can vary by roughly 50% over a 2 mm span.

Table 3-2: Dependence of Mo-Mo_2C resistivity on cross-sectional area for fixed resistance (0.704 Ω) and fixed line length (59.9 mm) over a 2 mm span

Position [mm]	Cross-Sectional Area [μm^2]	Resistivity [$x10^{-10}$ ohm-m]
0.0	32.67	3.84
0.4	42.04	4.94
0.8	29.87	3.51
1.2	36.92	4.34
1.6	34.65	4.07
2.0	44.68	5.25
Max-Min	**14.81**	**1.74**

3.4.4. Lead Wire Bonding Methods

Several bonding methods were attempted in an effort to find the most suitable way to fasten lead wires to the thermal spray sample as illustrated in Figure 3-4. After several failed experiments it was determined that the wire arc sprayed copper pads provided the best functionality.

Initially the welding method provided fair results however in order to obtain significant variations in resistance it was desirable to make ever thinner thermal spray deposits. The thin deposits, roughly 50 μm, proved to be detrimental to the welding process as there was not enough material to create a secure bond. This resulted in a relatively fragile connection which could be easily damaged in handling. The welding process also puts a large amount of

energy into a localized portion of the sample thus potentially damaging or altering the coating.

In terms of mechanical robustness the conductive epoxy worked well however, the results were questionable when using the epoxy. For example if the sample was strained and then released there was an uncertainty as to if the measured response was from the thermal spray material or a strain rate effect of the conductive epoxy. While it was not proved or disproved there was an underlying concern. When testing at low strain with low strain rates at room temperature the epoxy was a reasonable choice.

The wire arc spray method to deposit copper contact pads worked extremely well. Lead wires were able to be soldered directly to the pad resulting in a low resistance bond which was both mechanically and electrically stable. With the use of flame spray tape the sample could be masked allowing any size copper pad to be deposited.

3.4.5. Resistance as a Function of Strain

Resistance values for each Mo-Mo_2C line were normalized against initial resistance to allow for comparison. The normalized resistance as a function of strain is shown in Figure 3-13. From the plot it is clear to see that there is a hysteresis between the loading and unloading profiles. As the sample is loaded the resistance increases to a maximum at the maximum strain. Lines 2 and 3 follow a similar trend in that the resistance decreases over the entire unloading cycle, however, the resistance of line 1 begins to increase as the strain is relieved. Upon closer inspection the resistance of line 3 appears to reach a saturation point after which the resistance does not further decrease. It is unclear due to the noise of the data but it does not appear the resistance increases, certainly not to the same extent as what is observed for line 1.

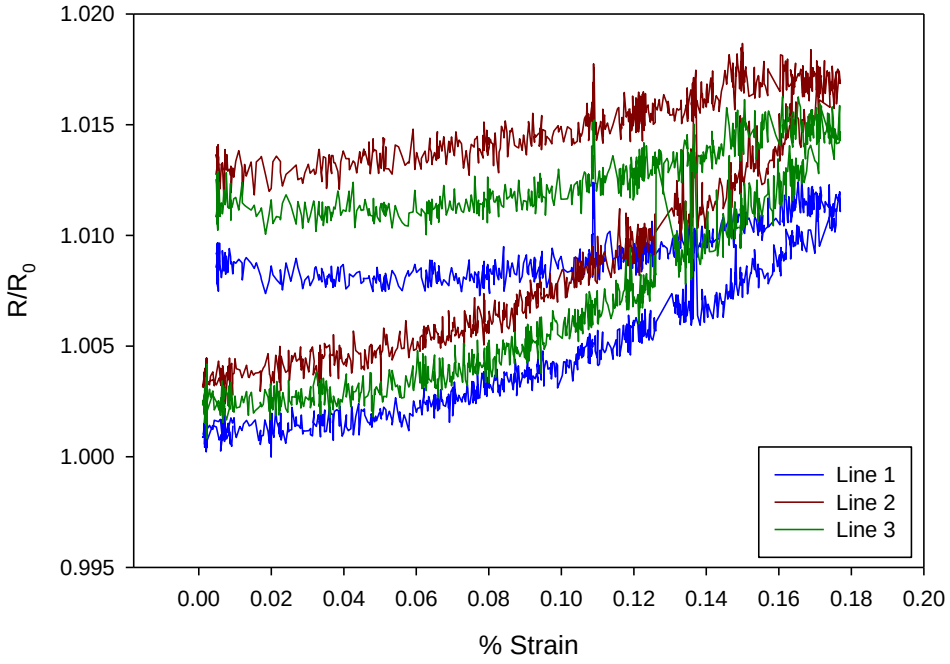

Figure 3-13: Normalized data from single strain cycle of APS Mo-Mo_2C on Spinel coated constant strain cantilever beam

In a bulk material, the applied tensile load would tend to increase the inter-atomic spacing of the lattice thus increasing the electrical resistance of the coating. In a thermal spray coating the tensile strain has the potential to affect the resistance through the "brick-like" structure in unique ways. While the tensile strain could act on the inter-atomic spacing it is also reasonable to assume the splat to splat bond is weaker than the atomic bonding, especially in the light of oxides, pores, and defects. Figure 3-14 shows a cross-sectional micrograph of a Mo-Mo_2C coating.

The fact that the resistance increases with increased strain could be a result of splats, or groups of splats, slipping against each other and thereby reducing the contact area between adjacent splats. With a reduced effective

contact area there would be a reduction in conduction paths and thus an increase in resistance.

Since the coating does not remain in the high resistance state there must be an elastic portion to the phenomenon. It is possible that the coating, already in tension due to the rapid solidification and shrinkage, finds stress relief mechanisms such as splat sliding due to the additional tensile strain imparted by the experiment. It may be the combination of residual stress and applied stress that is enough to cause splat slippage. Once the external strain is relieved there is still enough tensile stress in the coating which prevents the splats from returning to their initial positions. It is the residual tension, or lack of external compression, that results in the resistance increase over the duration of the experiment, i.e. offset in resistance from initial to final point.

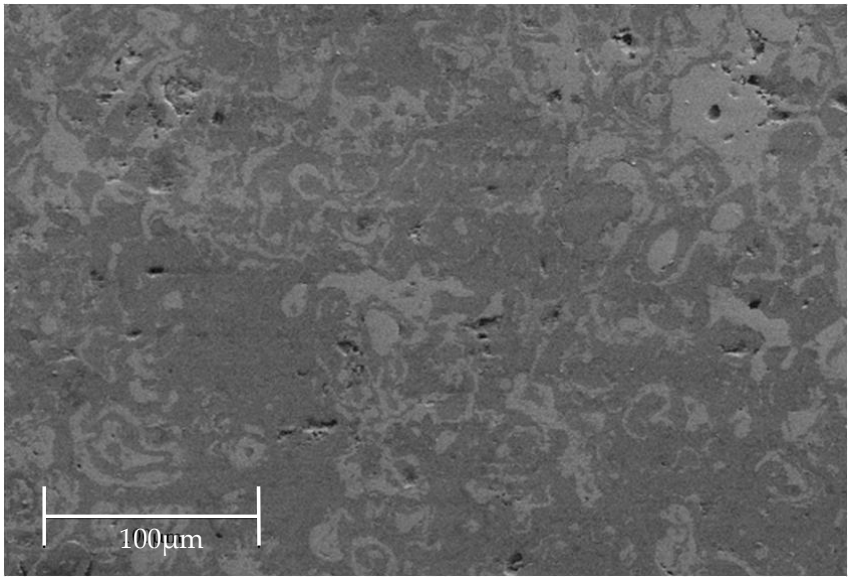

Figure 3-14: Cross-sectional micrograph of typical Mo-Mo_2C coating
[Image courtesy of W.B. Choi]

3.4.6. Resistance as a Function of Cyclic Strain

To better illustrate the relationship between resistance and strain several loading cycles were completed. All three test lines behaved identically, however for clarity only the raw data for line 2 is shown in Figure 3-15.

While somewhat of a trend can be seen in the raw data of Figure 3-15, Figure 3-16 shows the smoothed data broken into sections clearly showing increasing and decreasing strain through each test cycle of line 2.

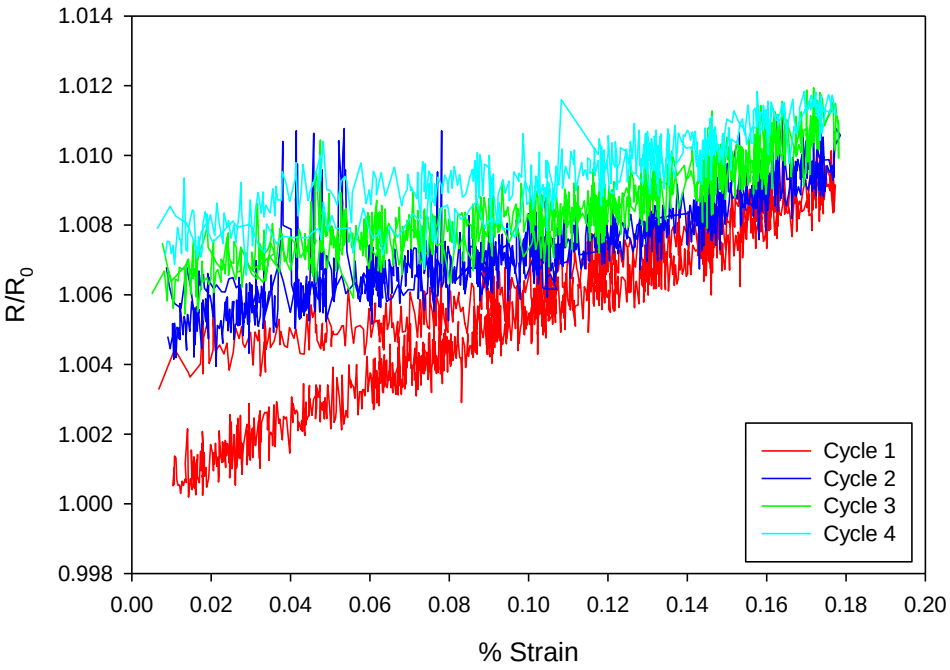

Figure 3-15: Normalized data of Mo-Mo_2C line 2 through four strain cycles

The data shown in Figure 3-16 supports the hypothesis set forth based on the single strain experiment. The resistance of the Mo-Mo_2C sample increases with strain to a common maximum point. Upon unloading the resistance decreases after which the sample exhibits increased resistance relative to the starting point. As discussed in 3.4.6 the splats slip against each other and thereby reduce the inter-splat contact area causing a decrease in conduction paths. When the strain is relieved there is an elastic portion which recovers allowing the splat to splat contact area to increase thus causing a decrease in resistance. Due to residual tensile stress the splats are unable to slip back to their

initial positions. This effect is displayed for each strain cycle however, the change in resistance from initial to final decreases as the number of cycles increase. Since the maximum applied strain is constant one can imagine that each strain cycle preferentially causes slippage at the weakest splat to splat interface. Once the splat slips the relaxation of the strain is not enough of a driving force to cause a slip reversal. Over time the cyclic strain would use all of the low energy interfaces and eventually not be able to overcome the splat to splat bond to cause slippage. At that point the cycle should be nearly reversible.

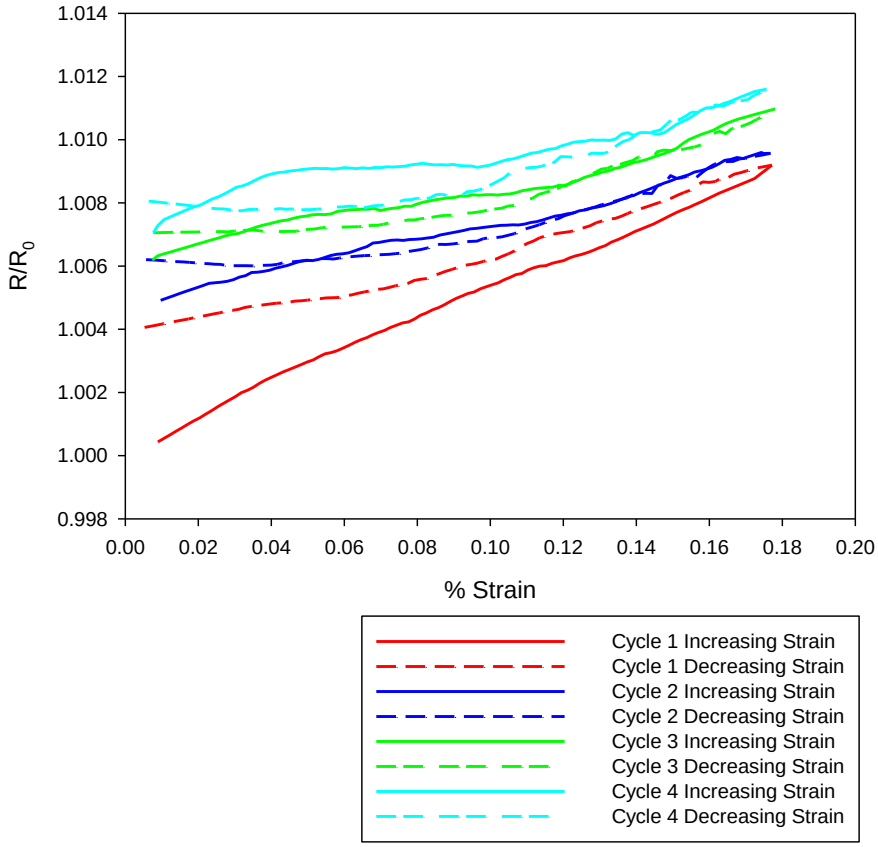

Figure 3-16: Smoothed data of Mo-Mo_2C line 2 though four strain cycles

Additionally it can be seen from Figure 3-16 that there is a phenomenon taking place after the first strain cycle. That is the resistance upon unloading temporarily decreases below the loading curve. It is also apparent that the area between the loading and unloading curves increases as the number of cycles increase.

If the first strain cycle is responsible for causing nonreversible slip in the low energy splat to splat interfaces, as shown by the large difference in initial and final resistance, subsequent strain cycles would act on the next weaker set of defects. It is possible that at some point the splat to splat interfaces are stronger than say a microcrack already in the system. Subsequent cycles could then cause crack opening and closing. If the remainder of the coating was well adhered the continual strain cycling could lead to crack propagation.

3.4.7. Variation of Resistance over Time at Constant Strain

The results of the time dependant creep test are shown in Figure 3-17. The three lines behaved identically so for clarity the response of line 2 is shown. Raw data is shown as scatter points in which smoothed data is superimposed. It is clear that the line has not sustained significant damage as the loading profile and hysteresis are nearly identical to that observed in the first cycle of Figure 3-16.

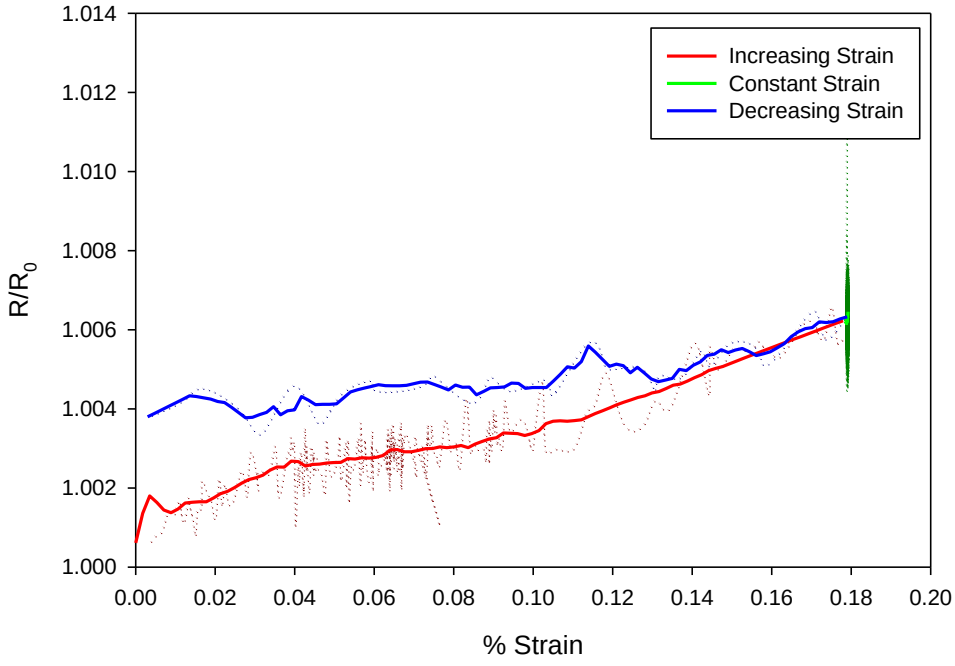

Figure 3-17: Raw and smoothed data for the time dependant creep experiment

Figure 3-18 shows the constant strain portion of the experiment where the normalized resistance is plotted as scatter points over the 5 hour duration. It can be seen that the normalized resistance only varies slightly over the course of the experiment. The absolute fluctuation of the resistance over the duration of the experiment is less than 2%. This variation can most likely be accounted by the change in ambient air temperature. It is not clear that there is a room temperature time dependant creep.

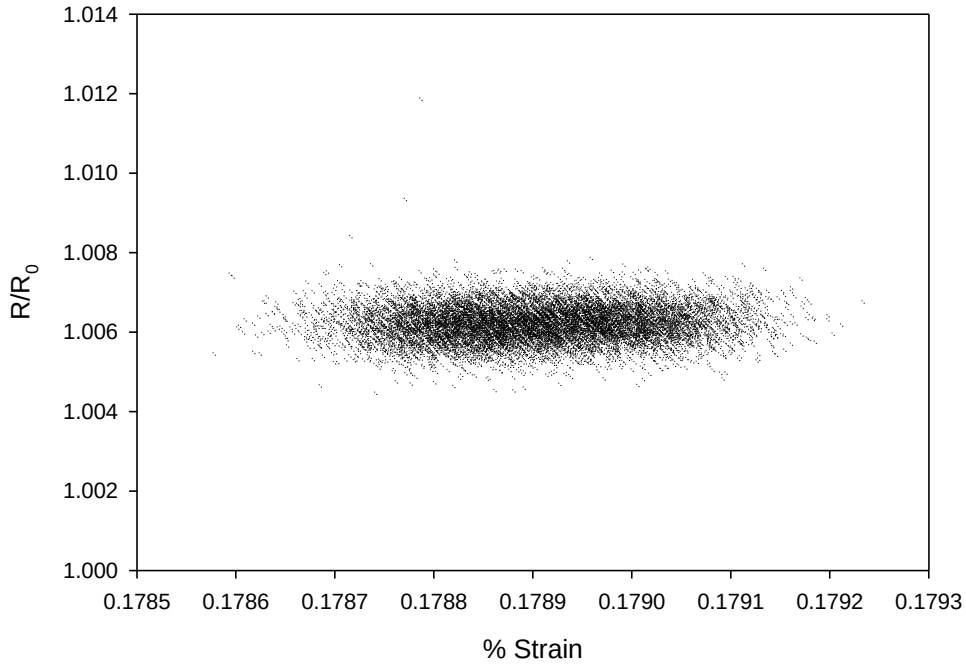

Figure 3-18: Variation in normalized resistance of line 2 over five hours at constant strain

3.5. Conclusion

In this chapter the ability to use electrical response coupled to mechanical strain via bending was demonstrated. A suitable setup was created allowing the future characterization and continued development of various other thermal spray materials. Building from the data collected for a Mo-Mo_2C thermal spray coating deposited via APS the following conclusions are drawn;

(a) Variations in the thermal spray coating have been shown to lead to sources of resistivity error. When evaluating samples based on changes rather than absolute values discussions in terms of resistance are suitable.

(b) Wire arc sprayed coppers pads allowed direct connection of measurement lead wires. Both mechanically and electrically robust, soldered connections offered greater functionality compared to welded or conductive epoxy mounted leads.

(c) A single strain cycle can provide insight as to the splat to splat bonding as indicated by the offset from initial to final resistance values.

(d) Multiple strain cycles provide a greater understanding of splat to splat slippage as well as the correlation to crack opening and closing phenomenon.

(e) Room temperature time dependant creep resistance may be a suitable test for some materials but for a well bonded structure it does not provide significant information.

Chapter 4: Electrical Response as a Function of Thermal Loading

4.1. Introduction

It is well known that the resistance of a bulk material increases as a function of temperature [34, 35]. This phenomenon has mainly been attributed to the scattering of electrons due to local vibrations of the lattice structure [36, 37]. While this trend has been seen several times in a variety of bulk materials it is desirable to see the effects of temperature on resistance for a material which does not necessarily behave as bulk. Being that the thermal spray coating is composed of splats which are built up to form a coating, both the interfacial and inter splat properties combine to produce a response which is often quite different than the bulk material.

In order to observe the change in resistance of the thermal spray coating as a function of temperature it was necessary to isolate the coating under test from the metallic substrate. This was accomplished by the deposition of an insulating ceramic layer as will be described shortly.

The addition of the insulating layer, while a necessary step, adds a degree of complication to the experiment. The substrate can no longer be described as a single member; it now has to be treated as a bi-layer system. As previously demonstrated the resistance of the thermal spray coating varies as a function of strain. Due to the bi-layer beam there will be an induced strain caused by the thermal mismatch between the coating and substrate. It is necessary to account for the thermal strains in order to ensure the resistance variations are caused purely by the thermal excitation and not due to mechanical influences.

Advanced systems consisting of multiple layers have been used extensively in a range of applications from microelectronics to structural

components. Throughout such widespread use, the thermal stresses in multilayered systems have been carefully examined [38].

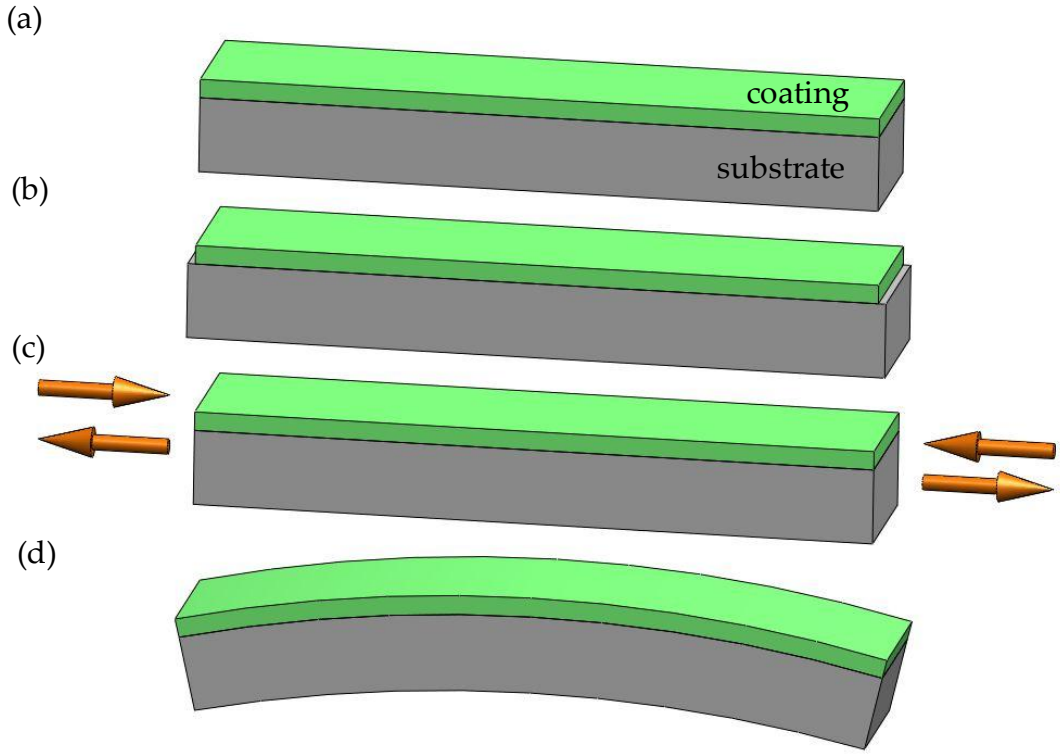

Figure 4-1: Schematics showing the bi-layer beam undergoing bending due to thermal stresses: (a) stress-free condition; (b) unconstrained strains due to temperature change; (c) constrained strain; and (d) strain induced bending caused by asymmetric stresses.

It has been demonstrated that for a bi-layer system, as shown in Figure 4-1, the total strain due to the thermal stresses in elastic multilayer systems can be given by [39].

$$\epsilon = c + \frac{t_c - t_b}{r}$$

Equation 4-1

where: c = uniform strain component

t_c = coating thickness

t_b = position of bending axis

r = radius of curvature for the system

For a system containing a homogeneous substrate and a single coating the uniform strain component is given by

$$c = \frac{(E_s t_s \alpha_s + E_c t_c \alpha_c)\Delta T}{E_s t_s + E_c t_c}$$

Equation 4-2

where: E_s = elastic modulus of substrate

t_s = substrate thickness

α_s = coefficient of thermal expansion of substrate

E_c = elastic modulus of coating

α_c = coefficient of thermal expansion of coating

For a single coating layer the position of the bending axis is given by

$$t_b = \frac{-E_s t_s^2 + E_c t_c^2}{2\,(E_s t_s + E_c t_c)}$$

Equation 4-3

4.2. Sample Preparation

In preparation for coating a 1" x 9" aluminum beam was grit blasted using a 40 μm diameter grit at 40 psi to both roughen the surface and provide a chemically active interface for the coating to bond. An insulating layer of yttria stabilized zirconia (YSZ) was deposited to a thickness of 350 μm via APS to ensure sufficient isolation. The YSZ was deposited with the Sulzer Metco F4 plasma spray torch using Saint Gobain 9204 powder as outlined in Table 4-1.

Nickel was sprayed onto the YSZ coated aluminum beam via HVOF through a shadow mask, as in the previous experiment. A JetKote HVOF torch and Metco 56F-NS powder were used. The shadow mask allowed for the deposition of three independent lines of roughly 60 mm length and 1 mm width. An overview of the HVOF deposition parameters are shown in Table 4-2.

Once the nickel was deposited copper pads were sprayed on the end of the nickel lines using wire arc spray. The sample was masked using flame spray tape such that the copper pads were roughly 2 mm x 2 mm in size. Lead wires were then soldered directly to the copper using the four wire arraignment discussed previously in section 3.3.3. Two adhesive backed K-type thermocouples were mounted to the aluminum beam to facilitate temperature measurement. One was connected to the Keithly meter to provide resistance-temperature information while the other was connected to the ECP computer to allow for the determination of the temperature-curvature relationship.

Table 4-1: Deposition parameters for YSZ insulator on aluminum beam via APS

Material	Ar slpm	H2 slpm	Gun I Amp	Gun V Volt	Carrier/ Flow slpm	Feedrate g/min	Spray Dist mm	Raster Speed mm/s
YSZ	47.5	6.0	550	61	Ar/3.0	30	100	500

Table 4-2: Deposition parameters for nickel lines on insulated beam via HVOF

Material	Hydrogen slpm	Oxygen slpm	Carrier/ Flow slpm	Feedrate g/min	Spray Dist mm	Raster Speed mm/s
Ni	560	210	Ar/28	40	175	500

4.3. Experiment

The Center for Thermal Spray Research of Stony Brook University has developed an array of customized sensors specifically suited for the thermal spray industry. One such system is the Ex-Situ Coating Property Sensor, termed ECP. The ECP sensor allows the determination of residual stress and various other material properties based on the curvature-temperature response of a bi-layer beam.

The ECP consists of a water cooled enclosure which houses three laser displacement sensors. The front face of the sensor serves as a sample holder to which a 1" x 9" beam is mounted. The ECP sensor slides into the cuff of a furnace such that the sample beam enters the furnace where it is heated uniformly. Three laser displacement sensors, located within the cooled enclosure, measure the deflection of the beam. A data acquisition system connected to a computer allows real-time temperature monitoring as well as calculation of curvature caused by the thermal expansion mismatch between the beam and the coating.

The prepared beam was mounted to the ECP and heated to 160°C. Once the temperature reached steady state the furnace was turned off and the sample allowed to cool to room temperature. This process was repeated several times in order to see any cyclic effects in the resistance as well as hysteresis. Curvature-temperature data was collected using the ECP while the Keithley 2700 digital multimeter was used to record resistance.

4.4. Results and Discussion

Initial testing showed that the solder method for connecting lead wires to the thermal spray lines had limitations. During heating the solder softened at roughly 185C resulting in diminished electrical contact resulting in ultimate failure.

4.4.1. Heating Profile Effects

Prior to experimentation, the ECP furnace was heated to 100C and allowed to cool to room temperature to bake out any residual moisture. The sample was then loaded onto the ECP and slid into the furnace where the sample was heated to 165°C. As the furnace controller was unable to allow a programmed ramp rate heating occurred in roughly 21 minutes. Once the temperature reached the set point the furnace was turned off and shortly thereafter the ECP was unloaded such that it could convectively cool to room temperature in ambient air. The profile of a single heating cycle is shown in Figure 4-2.

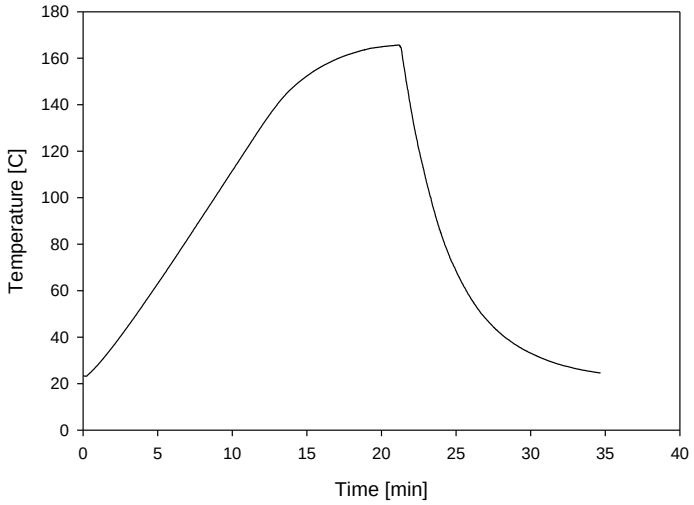

Figure 4-2: Temperature profile of experiment

The resistance was measured through five such heating cycles. The normalized resistance for the first four heating cycles is shown in Figure 4-3. As in previous experiments all three lines were in good agreement so for clarity the normalized resistance of line 2 is shown.

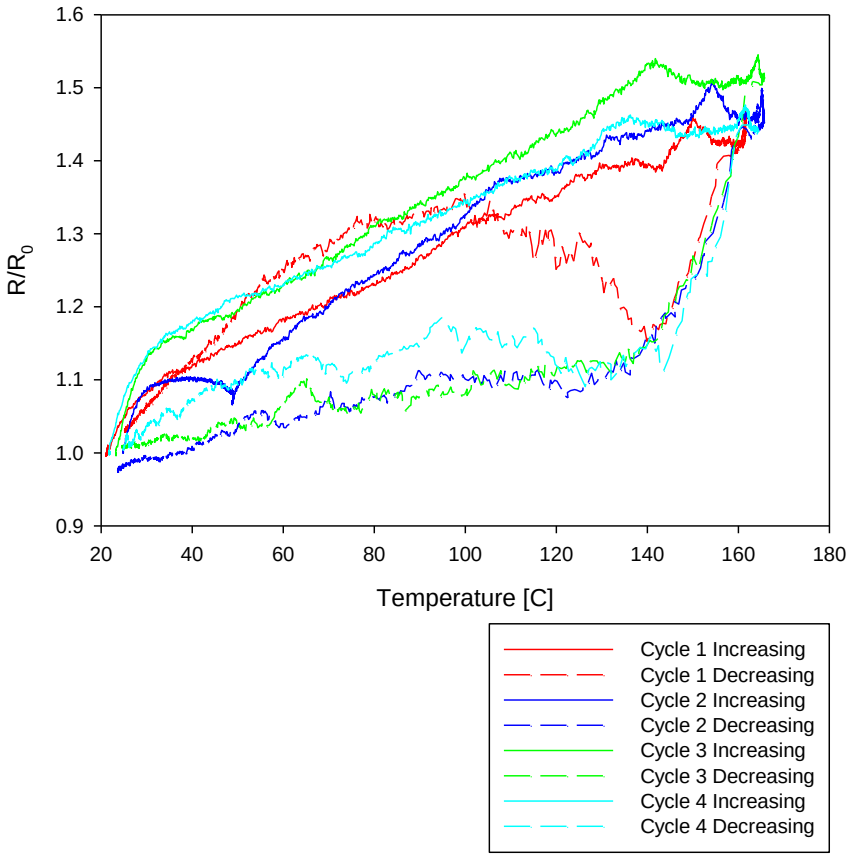

Figure 4-3: Normalized resistance of HVOF sprayed nickel line over four heating and cooling cycles

From Figure 4-3 it is clear that after the first heating cycle the resistance follows similar profiles. The inconsistency during the increasing portion of cycle 2 was due to a system error. Upon completion of cycle 1 the ECP was loaded into the furnace for cycle 2. The set point was not accepted by the temperature controller and thus the furnace did not heat appropriately. Once noticed it was

correct and heating began. After approximately 110°C the resistance behaved as indicated by both past and future cycles.

After the 4th temperature cycle the ECP was loaded once more, however, after the system reached 165°C the furnace was turned off and the sample left inside the furnace to cool over 8 hours. The main thought behind the additional test is that the thermocouples are mounted to the rear of the aluminum beam. It takes a greater amount of time for the aluminum beam to reach a steady state temperature than a thin line on the front surface of the beam, due to the large surface to volume ratio of the thin line. The thought was that while the thermocouples are providing surface temperature measurement they can be significantly different than the temperature of the sprayed nickel line. Figure 4-4 shows the results of the slow cooling experiment as well as the cooling from cycle 4 for comparison.

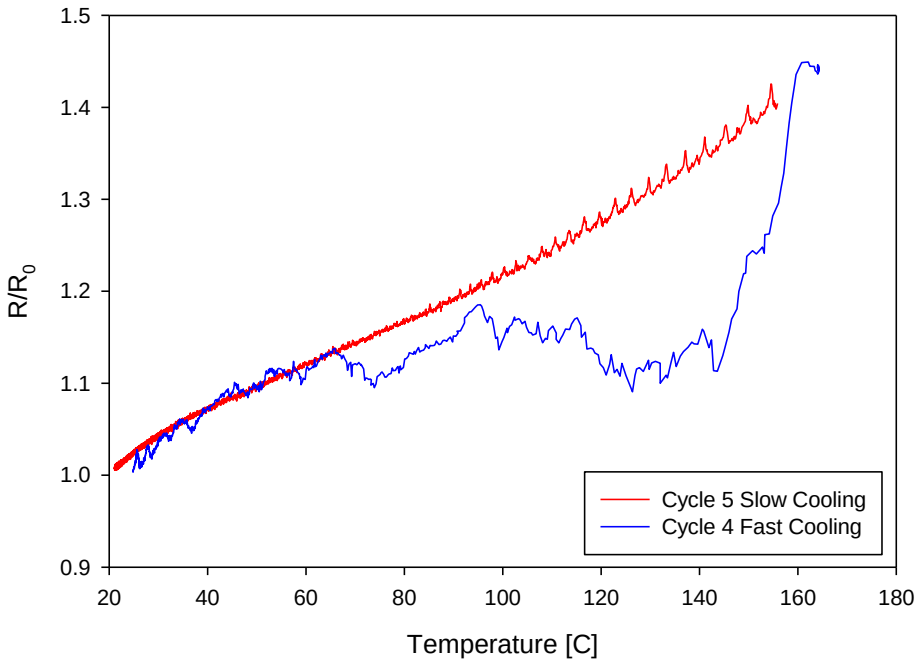

Figure 4-4: Comparison of normalized resistance of HVOF sprayed nickel line when cooled quickly (20 minutes) compared to cooled slowly (12 hours)

From Figure 4-4 it is clear that the cooling rate has a significant impact on the resistance of the thermal spray line. The cooling of cycle 5 was limited by the thermal losses of the furnace and is relatively linear from elevated to room temperature. Evaluated from 155°C to 145°C the furnace provided a cooling rate of 0.01°C/sec. Cycle 4 was able to cool much faster as the differential temperature between the sample and the environment was over 140°C resulting in a cooling rate of 0.70°C/sec over the range of 155°C to 145°C. The cooling rate of cycle 4 was over 50 times that of cycle 5.

The discontinuities in the profile of cycle 5 shown in Figure 4-4 are due to the cooling method used in the ECP sensor. Compressed air is used to limit the temperature inside the enclosure and thus protect the laser displacement sensors. The flow of air is proportional to the pressure in the reservoir of the compressor. Flow decreases as pressure decreases until the compressor turns on thus building pressure in the reservoir. This cycle repeats every six minutes and is in perfect agreement with fluctuations shown in Figure 4-4.

While the greatest effect can be seen in the cooling from 165°C to 140°C the cooling dependence is significant throughout the test. Less obvious would be the resistance effect during the heating cycle. Since the furnace is unable to provide for a controlled ramp once a set point is given the output power of the furnace reaches 100% during initial heating. Careful inspection of Figure 4-3 shows a large slope in the normalized resistance as the furnace begins heating. Opposite to that of cooling the thermal spray line has the tendency to heat before the beam reaches equilibrium.

Due to a limitation of the furnace controller the set point was manually adjusted to provide several dwell times as shown in Figure 4-5.

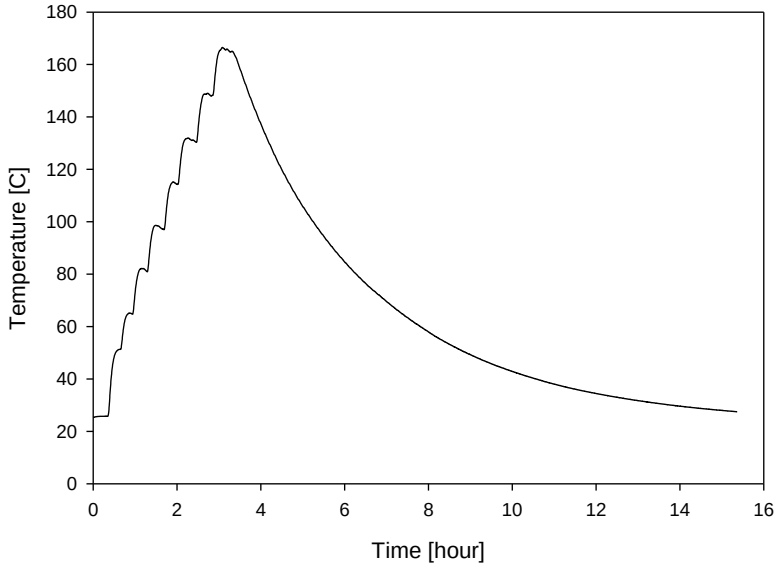

Figure 4-5: Temperature profile of the slow heating-slow cooling experiment.

Figure 4-6 and Figure 4-7 show the normalized resistance of line 2 over cycle 1 and cycle 2 respectively. Here the normalized resistance is plotted against thermal strain according to Equation 4-1. It should be noted that the inflection at approximately 0.0004% strain is caused by unloading the ECP from the furnace at roughly 40°C in order to prepare for the second cycle. From Figure 4-6 and Figure 4-7 there is clearly a linear relationship between normalized resistance and strain. At each point in the heating profile corresponding to a dwell time the increasing and decreasing paths connect showing that there is no, or very little, hysteresis in the system.

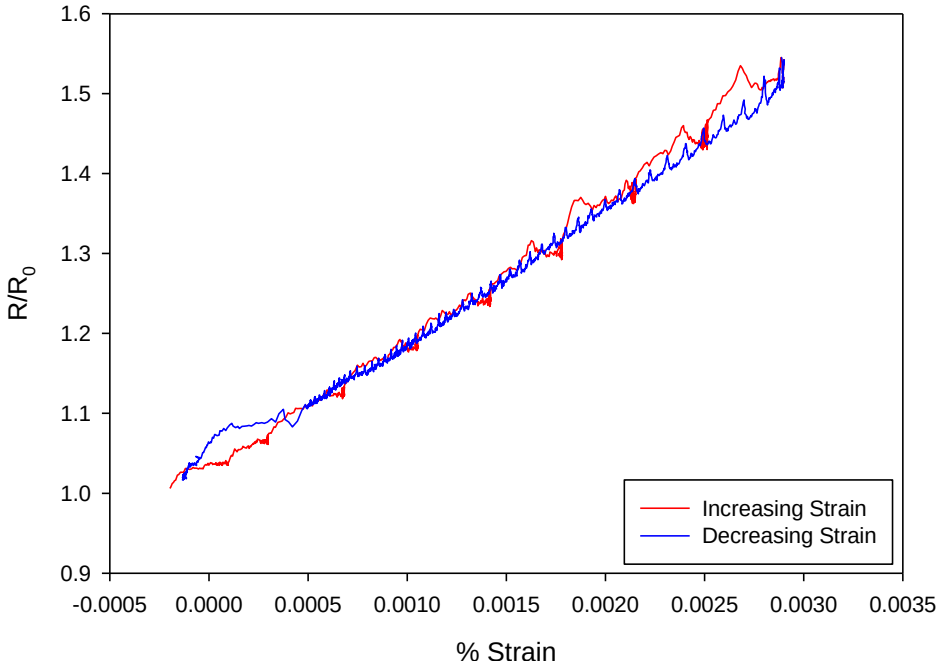

Figure 4-6: Normalized resistance of the HVOF sprayed nickel line over the first heating and cooling cycle

Figure 4-8 shows the curvature of the beam as a function of thermal strain. Again it is noted that at the dwell points of the heating profile the increasing and decreasing paths nearly connect. In this experiment the lead wires were directed outside of the furnace to the data acquisition system. It is likely that the wires themselves provided a small stress on the beam thus effecting curvature.

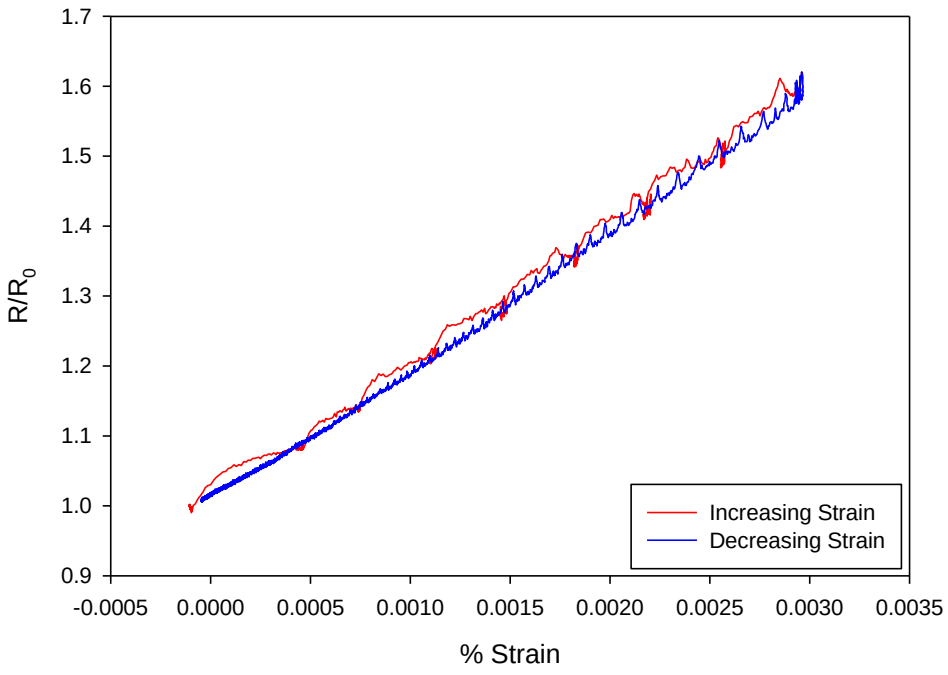

Figure 4-7: Normalized resistance of the HVOF sprayed nickel line over the second heating and cooling cycle

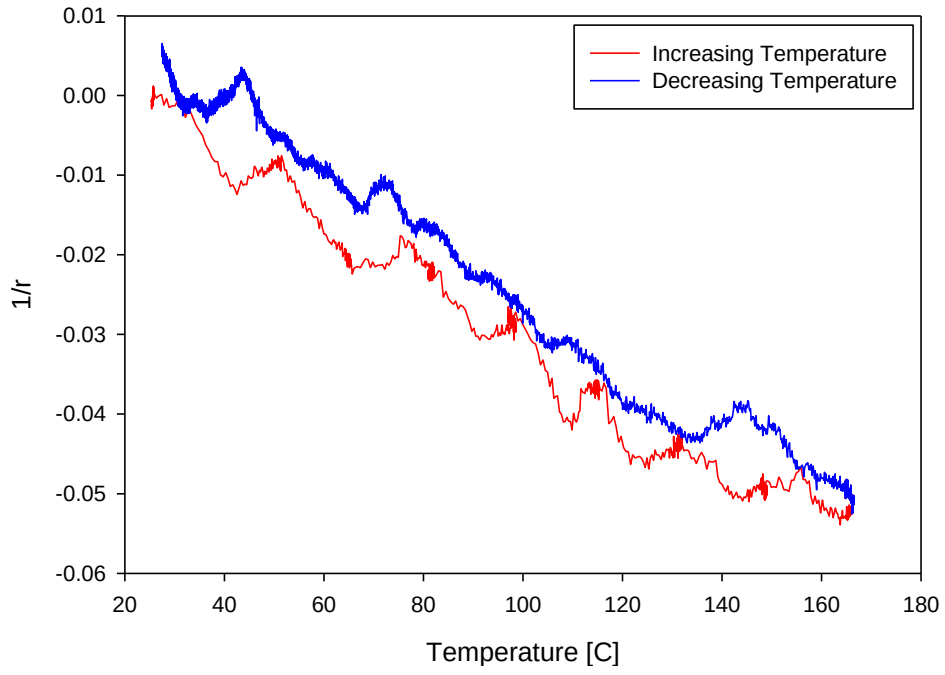

Figure 4-8: Curvature of the bi-layer beam through heating and cooling

On a final note in this analysis the thermal spray line under test was not considered as a strain inducing coating. This assumption was considered proper because of two facts. First the thickness of the line, 50 μm, is small compared to the thickness of the ceramic coating and the thickness of the beam, 350 μm and 1.6 mm, respectively. Secondly, there are three lines which are each roughly 1 mm x 60 mm for a total of 180 mm^2 compared to 5,800 mm^2 for the beam and ceramic coating.

4.5. Conclusion

An understanding of the coupling between thermal loading and electrical resistance was attempted. A system was created to measure electrical response as a function of temperature; however, there were several shortcomings. The following conclusions were determined:

(a) While wire arc sprayed copper pads and soldered lead wires worked well in previous testing the operating range posed a crippling limitation when attempting to couple resistance to thermal loading.

(b) Increased temperatures are necessary for determining response. Low temperature testing only shows that the resistance increases with temperature.

(c) The current experiment revealed no hysteresis in the resistance versus strain profile, however, this may be due to a limitation caused by the low temperature test.

(c) The limited data collected showed indisputably that the electrical response is heavily dependent on heating and cooling rates. Future testing must be carried out at reduced rates or ideally through system equilibrium points.

Chapter 5: Electrical Response as a Function of Elongation

5.1. Introduction

While Chapter 3 demonstrated the electrical response of a thermal spray coating through bending the experimentation was restricted to remain within the linear elastic portion of the cantilever beam. It is desirable to determine how the unique structure of a thermal spray coating behaves at high strain. Utilizing a polymeric substrate will allow higher strains to be achieved and thus provide greater knowledge of the thermal spray coating.

Figure 5.1 illustrates the present test where a polymer substrate with a deposited conductive line will be subjected to a uniaxial tensile force. The tensile force will create a tensile strain thus causing an elongation of the sample. Monitoring resistance during the test will help to develop new insight into the deposited coating through a coupled property response.

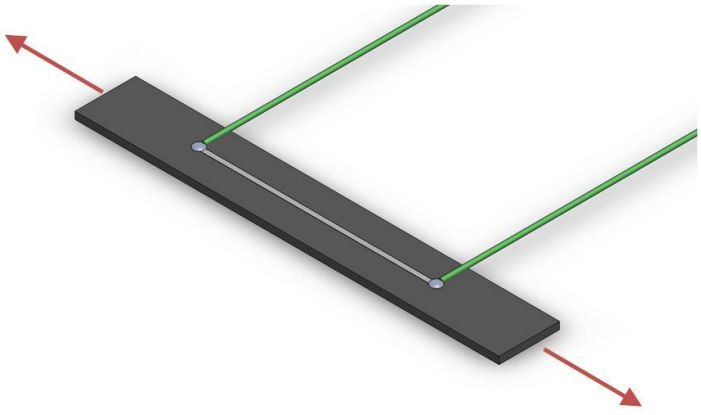

Figure 5-1: Schematic of high strain elongation test utilizing a two wire arraignment

5.2. Sample Preparation

The polymer substrate was created by depositing powder feedstock of polyethylene methacrylic acid (EMAA) onto a non-stick surface via flame spray. The copolymer deposit was built up to a thickness of 1.6mm over an area of roughly 1,000 cm^2. After deposition the polymer coating was peeled away from the non-stick surface yielding a free standing polymer film. Figure 5-2 shows an image acquired using a Zygo New View 200 White Light Interferometer Profilometer of the as sprayed EMAA surface.

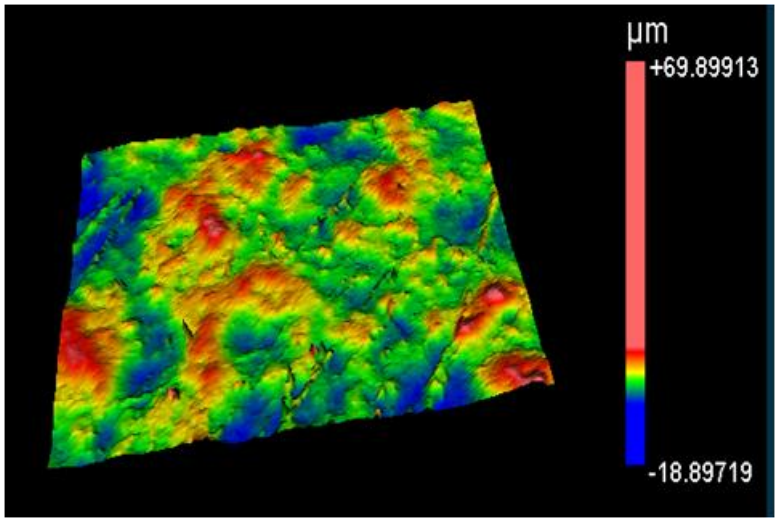

Figure 5-2: Illustration of EMAA polymer substrate prior to deposition

A conductive silver line was then sprayed directly onto the EMAA substrate using sub-sonic solid state deposition (S4D) without any additional surface preparation. Advanced Equipment Engineers AG-110 silver metal flake was used as the feedstock material which became entrained in a flow of helium and directed towards the substrate building the deposit. Through careful control of the process a silver line of approximately 18 µm height, 600 µm width, and 50 mm length was deposited in a direct write fashion without using masking. A brief outline of the deposition parameters is provided in Table 5-1. Figure 5-3

shows a 3D complied image taken of the deposited line using a Keyence HVX-500 Digital Microscope. The silver line is roughly 60 μm in width and 16 μm in height according to the scan.

To facilitate the measurement of resistance conductive epoxy was used to bond lead wires to the deposited silver line. Several samples were processed simultaneously where some were connected in the four wire arraignment discussed in section 3.3.3 while others were connected by the two wire method.

Table 5-1: Deposition parameters for conductive silver line sprayed onto EMAA substrates via S4D

Nozzle Size mm	Carrier Gas	Carrier Pressure psi	Feedrate g/min	Spray Dist mm	Raster Speed mm/min
0.4	Helium	300	0.3	10	560

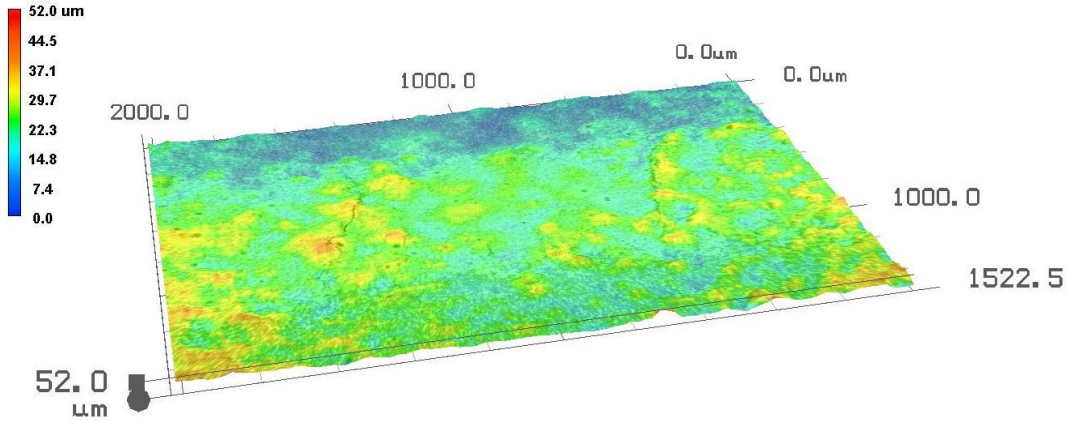

Figure 5-3: Illustration of S4D silver line on EMAA polymer. Silver line is roughly 16 μm in height and 600 μm in width.

5.3. Experiment

A computer controlled tabletop tensile tester, Interactive Instruments Model K1-16, was used to apply the tensile force to the sample as illustrated in Figure 5-4. The system was run in displacement mode such that the sample experienced a constant rate of elongation. The attached computer allowed the registering of displacement while a Keithley 2700 digital multimeter was used for resistance measurements.

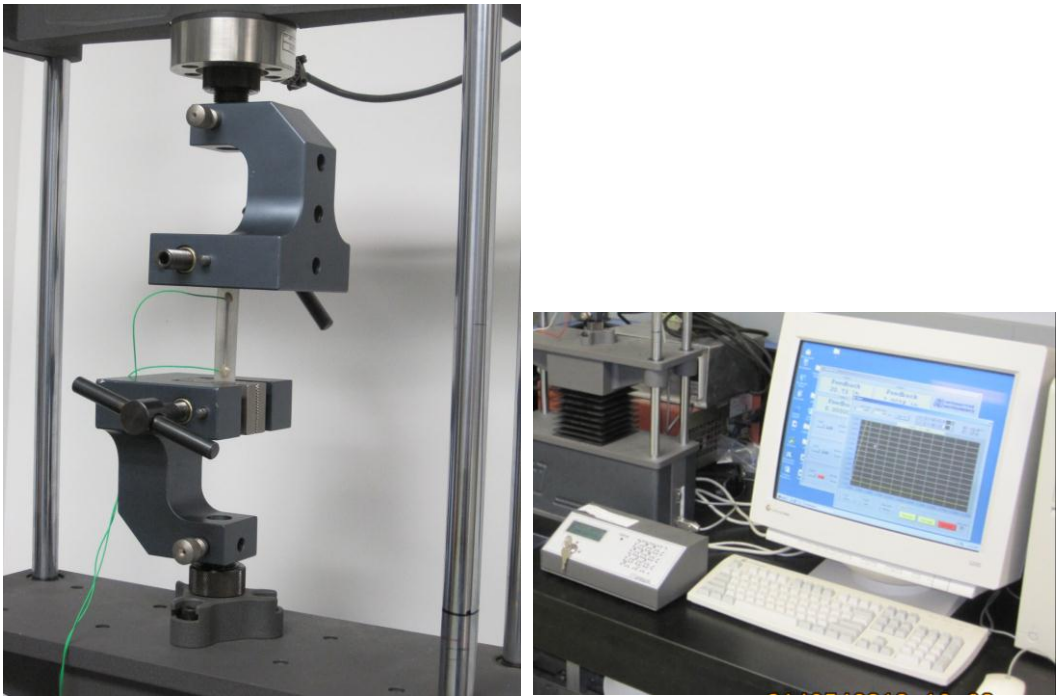

Figure 5-4: Illustration of tensile testing apparatus

5.3.1. Calculation of Strain

A beam subjected to an axial tensile force experiences a uniform tensile stress. As a result the sample experiences a uniaxial strain as given by Equation 5-1.

$$\epsilon = \frac{\delta}{L}$$

Equation 5-1

where: δ = elongation of the beam

L = initial length of the beam

Through the assumption that the polymer substrate does not slip within the grips of the tensile testing system the stroke of the grips can be substituted for the elongation of the beam thus allowing the calculation of strain. Since the polymer is relatively compliant, as compared to a metallic substrate, the approximation is reasonable and no slippage was observed throughout the experimentation. In an effort to further limit the possibility of slip the polymer was mounted such that the grips held a large surface area of the sample.

5.3.2. Resistance as a Function of Strain

The EMAA polymer sample with S4D sprayed silver line was mounted into the grips of the tensile tester. The Interactive Instruments K1-16 was programmed in a displacement mode to run a dual wave profile such that the sample would be subjected to a 10% strain then return back to the initial position.

The rate of displacement was programmed so both the loading and unloading paths would occur over four hours each thus yielding an eight hour experiment. The controller of the tensile tester collected time and displacement data while a Keithley 2700 digital multimeter registered the electrical resistance over time.

From previous test runs it was determined that the strain rate for EMAA is relatively low. The increasing strain does not appear to affect the polymer within reasonable rates. The problem arises during the relaxation step. Ideally the testing system would allow the polymer to naturally contract, perhaps against a small force to ensure a clean unloading profile. The current system requires a grip displacement rate be programmed for the increasing and decreasing strain. Relaxation times less than four hours for a 10% strain have shown signs of sample buckling.

5.3.3. Resistance as a Function of Cyclic Strain

While a single strain cycle can shed light on the response and reversibility of the coating a greater insight can be gathered from the cyclic response.

Once again the polymer substrate with the S4D deposited line was loaded into the tensile tester. The system was programmed with a triangular displacement profile causing the sample to experience a 2% elongation followed by relaxation back to the starting point. The rate of displacement was set so that one complete cycle would take four hours.

5.4. Results and Discussion

A scanning electron microscope (SEM) was used to examine the as sprayed S4D silver line. Figure 5-5 shows a top down view of the deposit where

there are no discernable defects such as cracks present. From the SEM image the silver line is roughly 950 μm wide, however, it is clear that there is no defined edge on which to base measurements.

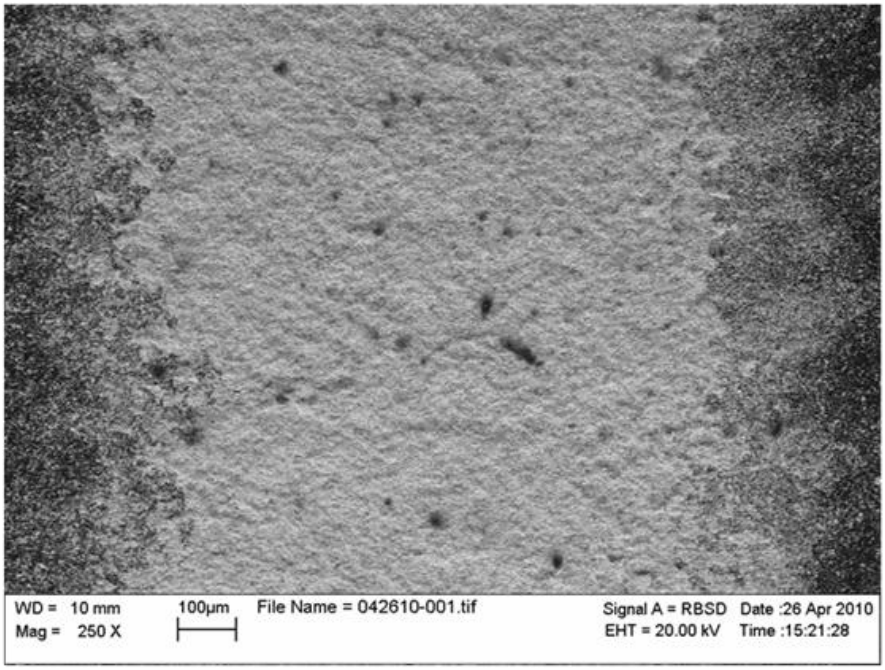

Figure 5-5: SEM image showing a top down view of as sprayed S4D silver line on EMAA copolymer

5.4.1. Resistance as a Function of Strain

Figure 5-6 shows the plot of both resistance and strain as a function of time for a single strain cycle of 10%. The first notable result is that the resistance appears to be rather linear as well as reversible all the way up to a 10% strain. As the resistance of the cycle is similar to that of the initial point it is reasonable to assume that no substantial plastic deformation took place.

To better show the reversibility, as well as to remove the time dependence, the normalized resistance is plotted against strain, as shown in Figure 5-7. Again, the small offset between the initial and final resistance implies that there was little damage done to the system.

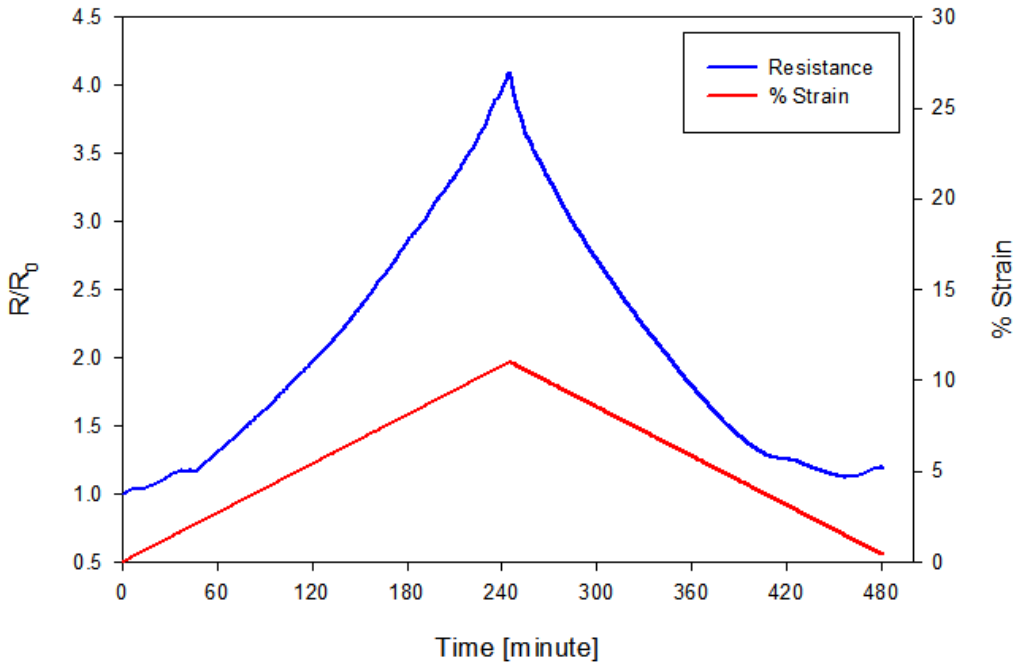

Figure 5-6: Illustration of resistance and strain as a function of time for the silver line deposited via S4D

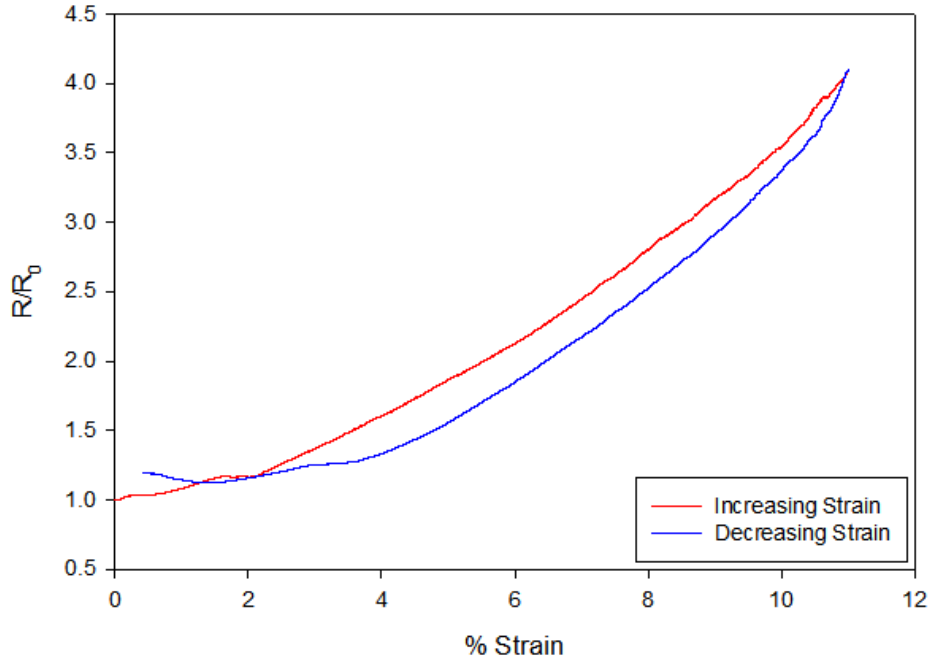

Figure 5-7: Illustration of resistance dependence on strain for S4D deposited line

Figure 5-8 shows an SEM image of the sample after loading. Despite the continuous electrical response and the slight offset of resistance at the conclusion of the experiment it is apparent that significant damage has taken place.

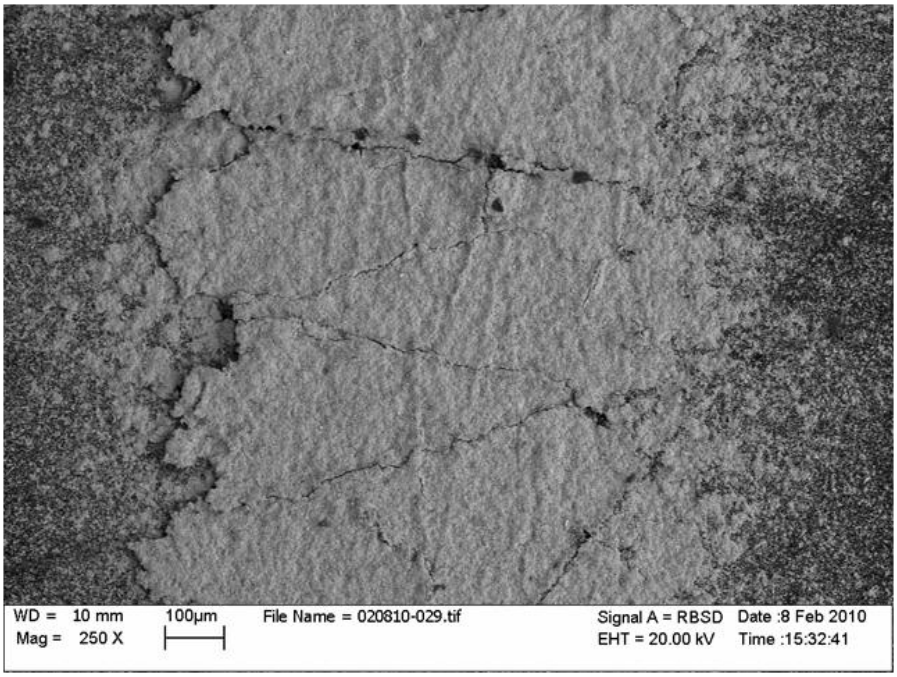

Figure 5-8: SEM image showing a top down view of the S4D silver line on EMAA copolymer after a single 10% strain load

As illustrated in Figure 5-8 there are several cracks which span the full length of the coating, however, their degree of separation varies along the crack. Some cracks show areas of clear separation while in others zones it appears as if there can be a conductive path. It was not possible to determine the crack depth into the surface of the coating. Based on how the resistance varied linearly and did not show an asymptote followed by an open circuit it is safe to say that the cracks did not penetrate significantly into the coating. Another possibility is that the line has a high enough conductance such that despite the crack a continuity path is present. It is also noticed that the cracks appear to be at angles of 20-25 degrees from the horizontal.

5.4.2. Resistance as a Function of Cyclic Strain

While the single strain loading experiment shows a reversible trend it is advantageous to determine the response over multiple cycles. Figure 5-9 shows the electrical response and strain as a function of time. The sample was loaded to 2% strain over 5 cycles.

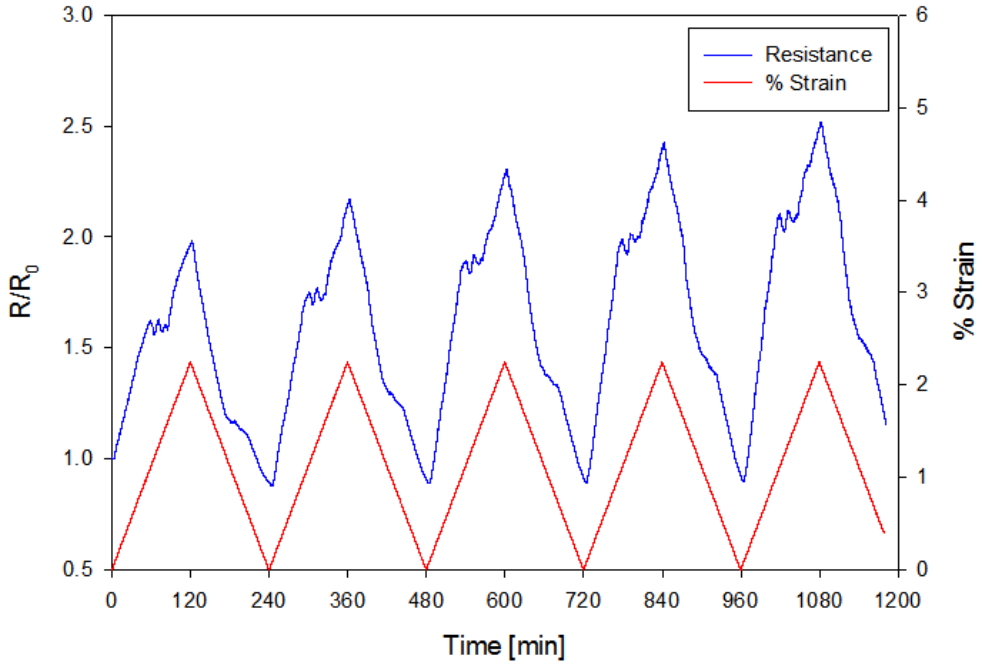

Figure 5-9: Plot of resistance and strain as a function of time

It is apparent that after the first cycle there is a resistance value to which subsequent cycles return. The value is slightly lower than the initial resistance of the line to which the data is normalized. While sample buckling was thought to be accounted for there may be a compressive effect if the sample does not relax at the same rate as the grips move towards each other during unloading.

Additionally, the maximum resistance of each cycle, corresponding to the maximum strain, increases with the number of cycles. In each cycle there is a disturbance just before the maximum strain is reached.

Figure 5-10 shows the normalized resistance as a function of strain. It is apparent that each cycle results in a slightly higher maximum resistance which implies that there is an increased amount of damage with each cycle.

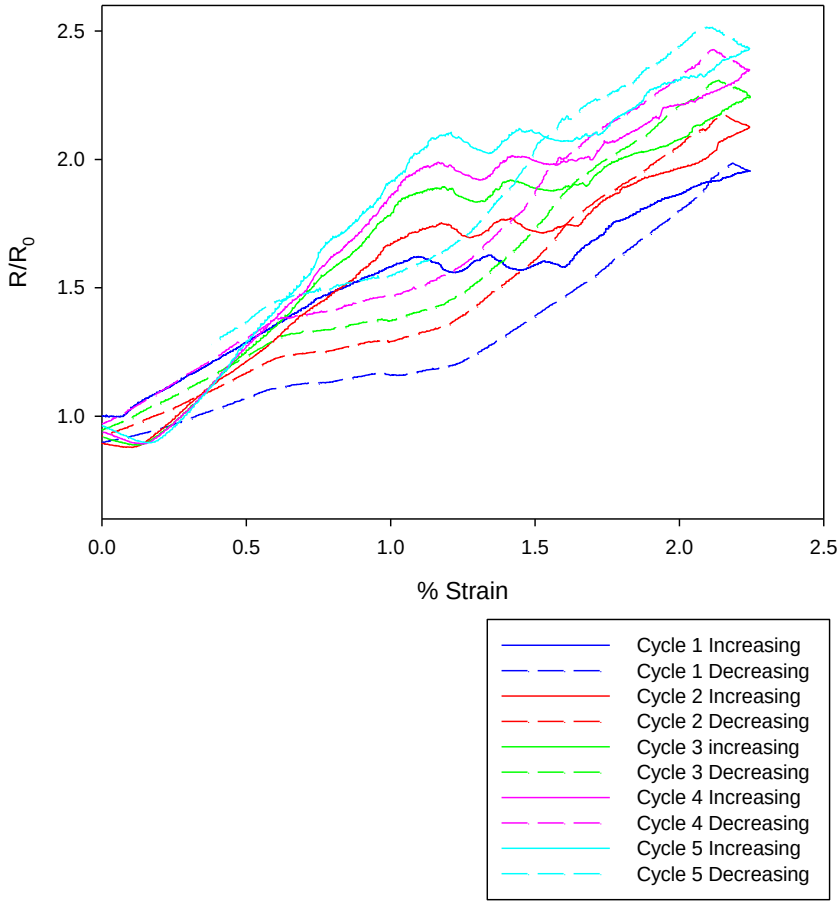

Figure 5-10: Plot of resistance as a function of strain for several cycles

Figure 5-11 shows a plot depicting the normalized resistance of each cycle at the maximum strain versus the number of cycles. The data point corresponding to the zeroth cycle was manually added under the assumption that if there never was a cycle the maximum normalized resistance would remain the initial normalized resistance and thus be 1. Despite the curve used to fit the

data it can be intuitively reasoned that there is some cycle number at which no more damage is imparted to the deposit due to cyclic loading.

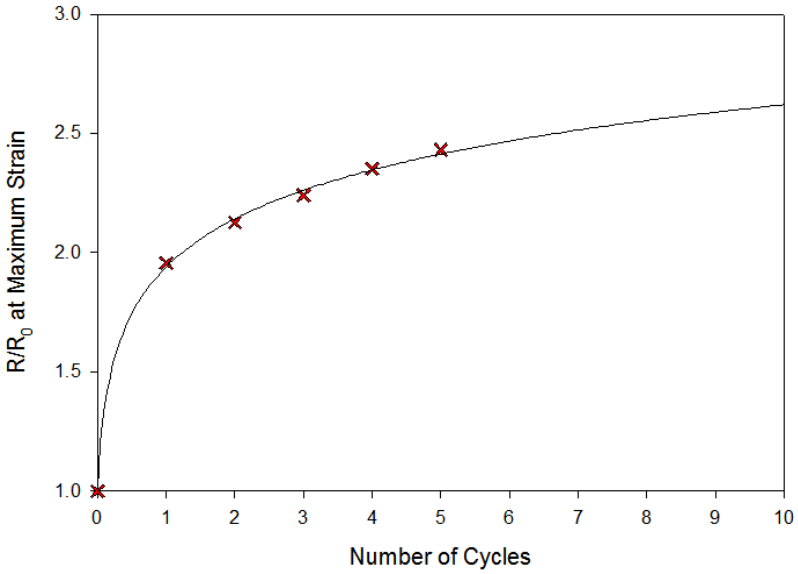

Figure 5-11: Plot of change in resistance against the number of cycles

Figure 5-12 shows an SEM image of the sample after five cycles of 2% strain loading. There are small but obvious cracks across the surface of the coating. The cracks tend to propagate perpendicular to the length of the line.

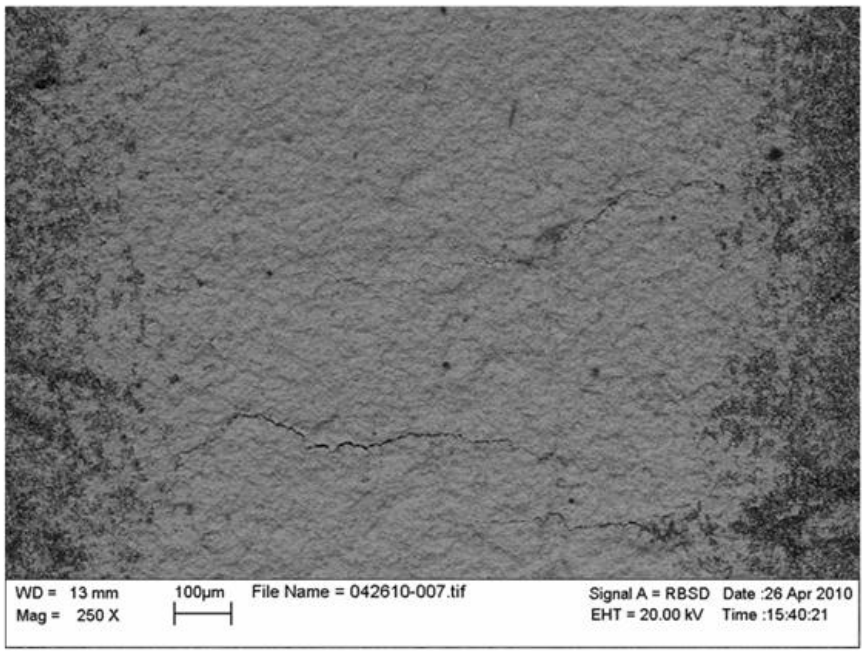

Figure 5-12: SEM image showing a top down view of a S4D silver line on EMAA copolymer after five cycles of 2% strain loading

5.5. Conclusions

The procedure used to determine the electrical response of a line deposited onto a polymer substrate via S4D was developed. Through several unique tests and spectroscopic characterization of the silver line the following conclusions have been established:

(a) The EMAA substrate with a silver line shows reversibility to strains as high as 10%. Increased strain loading has not been conducted to determine the upper limit.

(b) Despite the observance of significant cracking the sample appears to retain the linear response to 10% strain.

(c) At lower strain, 2%, the sample shows signs of reversibility as well as repeatability. Upon completion of the experiment some cracking could be seen.

(d) While only a preliminary finding, it is possible that a limit exists where, for a given strain loading, normalized resistance reaches a maximum and further cycles do not cause an increased response.

(e) Damage caused by high strain appears to cause cracking at roughly 20-25 degree angles while reduced strain causes cracking perpendicular to the length of the line.

Chapter 6: Summary

Emerging applications in electrical systems and components require the development of new and novel characterization methods for thermal spray coatings. As briefly outlined earlier the thermal spray process is complex with several multivariable dependencies and relations. For this reason it is not a simple task to optimize a given process.

It is necessary to develop new test methods which dynamically allow the determination of coating properties. Traditional mechanical properties are not sensitive to characterize and classify the electrical response of a material and there new methods must be developed to help fill the void in characterization methods related to sample electrical properties.

6.1. Methodologies to Measure Resistance and Electrical Properties

The present work served to demonstrate the feasibility of measuring the coupled property response of a thermal spray coating. Test platforms were created to facilitate the measurement of electrical resistance as a function of:

- Strain via Bending
- Strain via Tensile Load
- Thermal Loading

For each method a clear outline was presented as to the testing process and procedure. Several correlations were observed, such as splat to splat sliding,

thus allowing a greater understanding into the coating properties and microstructure.

The developed tests allowed for the creation of a new class of characterization methods based upon electrical responses which will provide a platform for the continued testing of samples.

6.2. Future Work

To gain a better insight as well as to improve the robustness of the test systems the following future work is suggested:

Electrical-Mechanical via Bending

- Increase the capabilities by characterizing lines on both sides of the beam thus allowing data to be collected for compression as well as tension

Electrical Thermal

- Improve the lead wire mounting method such that higher temperature testing can be accomplished

Electrical-Mechanical via Extension

- Develop the relation between strain rate and polymeric material to prevent substrate buckling upon unloading

References

1. Herman, H., *Plasma-Sprayed Coatings.* Scientific American, 1988. **259**(3): p. 112-117.

2. Herman, H., S. Sampath, and R. McCune, *Thermal spray: Current status and future trends.* Mrs Bulletin, 2000. **25**(7): p. 17-25.

3. Sampath, S. and X. Jiang, *Splat formation and microstructure development during plasma spraying: deposition temperature effects.* Materials Science and Engineering a-Structural Materials Properties Microstructure and Processing, 2001. **304**: p. 144-150.

4. Shaw, L.L., et al., *The dependency of microstructure and properties of nanostructured coatings on plasma spray conditions.* Surface & Coatings Technology, 2000. **130**(1): p. 1-8.

5. Sampath, S. and H. Herman, *Rapid solidification and microstructure development during plasma spray deposition.* Journal of Thermal Spray Technology, 1996. **5**(4): p. 445-456.

6. Sevostianov, I. and M. Kachanov, *Plasma-sprayed ceramic coatings: anisotropic elastic and conductive properties in relation to the microstructure; cross-property correlations.* Materials Science and Engineering a-Structural Materials Properties Microstructure and Processing, 2001. **297**(1-2): p. 235-243.

7. Khor, K.A., et al., *High temperature damping behavior of plasma sprayed NiCoCrAlY coatings.* Journal of Thermal Spray Technology, 2002. **11**(3): p. 359-364.

8. Harok, V. and K. Neufuss, *Elastic and inelastic effects in compression in plasma-sprayed ceramic coatings.* Journal of Thermal Spray Technology, 2001. **10**(1): p. 126-132.

9. Kulkarni, A., et al., *Comprehensive microstructural characterization and predictive property modeling of plasma-sprayed zirconia coatings.* Acta Materialia, 2003. **51**(9): p. 2457-2475.

10. Liu, Y.J., et al., *Anelastic Behavior of Plasma-Sprayed Zirconia Coatings.* Journal of the American Ceramic Society, 2008. **91**(12): p. 4036-4043.

11. Sevostianov, I. and M. Kachanov, *Modeling of the anisotropic elastic properties of plasma-sprayed coatings in relation to their microstructure.* Acta Materialia, 2000. **48**(6): p. 1361-1370.

12. Parthasarathi, S., et al., *Ultrasonic characterization of elastic anisotropy in plasma-sprayed alumina coatings.* Journal of Thermal Spray Technology, 1995. **4**(4): p. 367-373.

13. Sharma, A., et al., *Anisotropic electrical conduction from heterogeneous oxidation states in plasma sprayed TiO2 coatings.* Journal of Applied Physics, 2006. **100**(11): p. -.

14. Ohmori, A., et al., *Electrical-Conductivity of Plasma-Sprayed Titanium-Oxide (Rutile) Coatings.* Thin Solid Films, 1991. **201**(1): p. 1-8.

15. Nakamura, T. and Y.J. Liu, *Determination of nonlinear properties of thermal sprayed ceramic coatings via inverse analysis.* International Journal of Solids and Structures, 2007. **44**(6): p. 1990-2009.

16. Liu, Y., et al., *Non-linear elastic properties of plasma-sprayed zirconia coatings and associated relationships with processing conditions.* Acta Materialia, 2007. **55**(14): p. 4667-4678.

17. Rangaraj, S. and K. Kokini, *Time-dependent behavior of ceramic (zirconia)-metal (NiCoCrAlY) particulate composites.* Mechanics of Time-Dependent Materials, 2002. **6**(2): p. 171-191.

18. Choi, W.B., et al., *Indentation of Metallic and Cermet Thermal Spray Coatings.* Journal of Thermal Spray Technology, 2009. **18**(1): p. 58-64.

19. Kharas, B.D., S. Sampath, and R.J. Gambino, *Anisotropic resistivity in plasma-sprayed silicon thick films*, in *Journal of Applied Physics*. 2005. p. -.

20. Matejicek, J. and S. Sampath, *In situ measurement of residual stresses and elastic moduli in thermal sprayed coatings - Part 1: apparatus and analysis.* Acta Materialia, 2003. **51**(3): p. 863-872.

21. Clyne, T.W. and S.C. Gill, *Residual stresses in thermal spray coatings and their effect on interfacial adhesion: A review of recent work.* Journal of Thermal Spray Technology, 1996. **5**(4): p. 401-418.

22. Sampath, S., et al., *Role of thermal spray processing method on the microstructure, residual stress and properties of coatings: an integrated study for Ni-5 wt.%Al bond coats.* Materials Science and Engineering a-Structural Materials Properties Microstructure and Processing, 2004. **364**(1-2): p. 216-231.

23. Matejicek, J. and S. Sampath, *Intrinsic residual stresses in single splats produced by thermal spray processes.* Acta Materialia, 2001. **49**(11): p. 1993-1999.

24. Sampath, S., et al., *Sensing, Control, and In Situ Measurement of Coating Properties: An Integrated Approach Toward Establishing Process-Property Correlations.* Journal of Thermal Spray Technology, 2009. **18**(2): p. 243-255
184.

25. Pfender, E., *Fundamental-Studies Associated with the Plasma Spray Process.* Surface & Coatings Technology, 1988. **34**(1): p. 1-14.

26. Dykhuizen, R.C., et al., *Impact of high velocity cold spray particles.* Journal of Thermal Spray Technology, 1999. **8**(4): p. 559-564.

27. Choi, W.B., et al., *Integrated characterization of cold sprayed aluminum coatings.* Acta Materialia, 2007. **55**(3): p. 857-866.

28. Zhang, H., et al., *Studies of splat morphology and rapid solidification during thermal spraying.* International Journal of Heat and Mass Transfer, 2001. **44**(24): p. 4579-4592.

29. Li, J., et al., *Interdigital capacitive strain gauges fabricated by direct-write thermal spray and ultrafast laser micromachining.* Sensors and Actuators a-Physical, 2007. **133**(1): p. 1-8.

30. Chen, Q., et al., *Novel sensor fabrication using direct-write thermal spray and precision laser micromachnining.* Journal of Manufacturing Science and Engineering-Transactions of the Asme, 2004. **126**(4): p. 830-836.

31. Sampath, S., et al., *Thermal Spray Techniques for Fabrication of Meso-Electronics and Sensors.* Materials for Direct Write Electronics, Materials Research Society, 2005: p. 181.

32. Longtin, J., et al., *Sensors for harsh environments by direct-write thermal spray.* Ieee Sensors Journal, 2004. **4**(1): p. 118-121.

33. Prudenziati, M. and M.L. Gualtieri, *Electrical properties of thermally sprayed Ni- and Ni20Cr-based resistors.* Journal of Thermal Spray Technology, 2008. **17**(3): p. 385-394.

34. Heaney, M.B., *Resistance-expansion-temperature behavior of a disordered conductor-insulator composite.* Applied Physics Letters, 1996. **69**(17): p. 2602-2604.

35. Bhatia, A.B. and D.E. Thornton, *Structural aspects of the electrical resistivity of binary alloys.* Physical Review B-Solid State, 1970. **2**(8): p. 3004-3012.

36. Mayadas, A.F. and M. Shatzkes, *Electrical-Resistivity Model for Polycrystalline Films - Case of Arbitrary Reflection at External Surfaces.* Physical Review B, 1970. **1**(4): p. 1382-&.

37. Kittel, C., *Introduction to solid state physics*. 8th ed. 2005, Hoboken, NJ: Wiley. xix, 680 p.

38. Hsueh, C.H., *Thermal stresses in elastic multilayer systems.* Thin Solid Films, 2002. **418**(2): p. 182-188.

39. Hsueh, C.H. and A.G. Evans, *Residual-Stresses in Metal Ceramic Bonded Strips.* Journal of the American Ceramic Society, 1985. **68**(5): p. 241-248.